World Electric Vehicle Journal

MDPI

Article

A Novel Battery Temperature-Locking Method Based on Self-Heating Implemented with an Original Driving Circuit While Electric Vehicle Driving: A Numerical Investigation

Wei Li [1,2], Shusheng Xiong [2,3,*] and Wei Shi [3]

[1] Jiaxing Research Institute, Zhejiang University, Jiaxing 314031, China; liweisail@126.com
[2] Longquan Industrial Innovation Research Institute, Longquan 323700, China
[3] College of Energy Engineering, Zhejiang University, Hangzhou 310027, China; shiw@zju.edu.cn
* Correspondence: xiongss@zju.edu.cn

Abstract: In extremely cold environments, when battery electric vehicles (BEVs) are navigating urban roads at low speeds, the limited heating capacity of the on-board heat pump system and positive temperature coefficient (PTC) device can lead to an inevitable decline in battery temperature, potentially falling below its permissible operating range. This situation can subsequently result in vehicle malfunctions and, in severe cases, traffic accidents. Henceforth, a novel battery self-heating method during driving is proposed to maintain battery temperature. This approach is ingeniously embedded within the heating mechanism within the motor driving system without any necessity to alter or modify the existing driving circuitry. In the meantime, the battery voltage can be regulated to prevent it from surpassing the limit, thereby ensuring the battery's safety. This method introduces the dead zone into the space vector pulse width modulation (SVPWM) algorithm to form the newly proposed dSVPWM algorithm, which successfully changes the direction of the bus current in a PWM period and forms AC, and the amplitude of the battery alternating current (AC) can also be controlled by adjusting the heating intensity defined by the ratio of the dead zone and the compensation vector to the original zero vector. Through the Simulink model of the motor driving system, the temperature hysteresis locking strategy, grounded in the field-oriented control (FOC) method and employing the dSVPWM algorithm, has been confirmed to provide controllable and sufficiently stable motor speed regulation. During the low-speed phase of the China Light Vehicle Test Cycle (CLTC), the battery temperature fluctuation is meticulously maintained within a range of ± 0.2 °C. The battery's minimum temperature has been successfully locked at around -10 °C. In contrast, the battery temperature would decrease by a significant 1.44 °C per minute without the implementation of the temperature-locking strategy. The voltage of the battery pack is always regulated within the range of 255~378 V. It remains within the specified upper and lower thresholds. The battery voltage overrun can be effectively avoided.

Keywords: lithium-ion battery; extremely cold environment; internal self-heating; motor drive system

Citation: Li, W.; Xiong, S.; Shi, W. A Novel Battery Temperature-Locking Method Based on Self-Heating Implemented with an Original Driving Circuit While Electric Vehicle Driving: A Numerical Investigation. *World Electr. Veh. J.* **2024**, *15*, 408. https://doi.org/10.3390/wevj15090408

Academic Editor: Joeri Van Mierlo

Received: 29 July 2024
Revised: 29 August 2024
Accepted: 4 September 2024
Published: 6 September 2024

1. Introduction

In scenarios where battery electric vehicles (BEVs) are started and operated in exceptionally frigid conditions of -30 °C or colder, particularly when navigating urban roads at slow speeds, it is inevitable that, despite the battery's initial discharge at a minimal current, the overall battery temperature will decline or potentially drop beneath its acceptable operating threshold. At this time, the battery polarization increases, the voltage drops rapidly, and for the sake of battery life and safety, the battery management system (BMS) will limit the battery's ability to continue working, causing the vehicle to break down and even causing traffic accidents. Therefore, the battery must be heated while driving to restore its state of power (SOP). There are two main types of existing on-board heating technology solutions: the first is heat pump air conditioning. Lee et al. [1] showed that at

an ambient temperature of 10 °C, the coefficient of performance (COP) of the vehicular heat pump can reach 2.4. However, at an ambient temperature of −10 °C, a heat pump using a single heat source cannot work effectively, and the COP is close to 1. Heat pumps that can work in extremely low-temperature environments (below −20 °C) currently do not have a good industrial solution [2]. The second is adopting a heater composed of positive temperature coefficient (PTC) material, or an alternative dissipative resistor, to directly heat the circulating coolant, which in turn heats the battery. However, when the temperature drops, the battery frequently lacks sufficient state of power (SOP) to cater to the full power operation of the heater, which is around 4 kW in the case of mid-range passenger cars. Consequently, this approach to heating proves to be excessively sluggish or even impractical.

AC internal heating is a technology that relies on the internal materials of the battery to generate heat under the action of alternating current, which has the advantages of fast and homogeneous temperature rise, less heat loss to the surroundings, and no heating element is needed [3]. The increase in impedance of Lithium-ion (Li-ion) batteries at low temperatures is to the benefit of battery self-heating because, under the same amplitude of alternating current (AC), a larger amount of ohmic and electrochemical heat is generated inside the battery [4]. In the past ten years, many scholars have studied the low-temperature heating characteristics of batteries through AC power cabinets in the laboratory [3,5–12]. These research results verified the feasibility of battery self-heating technology. More importantly, these studies indicate that if the parameters of alternating current (amplitude and frequency) are properly selected to keep the battery terminal voltage within the upper and lower limits, heating lithium-ion batteries at extremely low temperatures using AC heating has been proven to be effective and benign. For instance, Ruan H et al. concluded that as long as the battery terminal voltage is controlled within its upper and lower limits, there will be almost no significant battery life degradation in the short term [13]. Guo S et al. studied the aging effects of repeated AC heating cycles on lithium-ion batteries at −20 °C through capacity calibration and incremental capacity analysis. These heating processes were always without overvoltage. The results showed no adverse effects on the cell's lifespan [14]. Additionally, the studies by Zhu J [3] and Jiang J [10] also reached the same conclusion. However, the above studies were realized under laboratory conditions and cannot be applied to the vehicle environment. Research in recent years has focused on how battery self-heating methods can be applied to vehicles. One scheme is to additionally design a separate part of the vehicle that is dedicated to battery self-heating [15–22]. Undoubtedly, this pattern increases the cost and weight of the vehicles. The other pattern is to integrate battery heating with a vehicle subsystem, in which the most promising method is to embed the heating strategy in the motor driving system. Most of these methods require changes to the topology of high-voltage wiring and are only applicable to newly developed vehicles [23–26]. In 2022, Du C. et al. proposed a battery internal heating method without any additional hardware modification in a cold environment [27]. However, this method can only be used for parking heating. So far, no research has been found on the battery self-heating method that can be used in the driving process without changing the original circuit topology of the vehicle, nor on the battery temperature control strategy with adjustable heating intensity.

To solve the problem of battery temperature drop during the driving of BEVs in extremely cold environments and fill the research gap in this direction, this paper proposes a new method for locking battery temperature during driving. The proposed method is entirely rooted in the existing motor driving system, mandating neither the integration of additional hardware nor alterations to the original circuitry; it aims to achieve battery self-heating exclusively by finely tuning control strategies. In consideration of the circuitry's inherent compatibility and suitability, it is expected to yield no adverse effects. By modifying the underlying strategy for motor control, the battery temperature is held higher than the set threshold, and the battery voltage is controlled so that it does not exceed the limit to ensure the safety of the battery. Thus, customers can obtain an enhanced driving experience, including an extended driving range in winter, with virtu-

ally no extra cost incurred from the vehicle purchase. The content of this paper mainly includes the following: firstly, the theoretical basis of the permanent magnet synchronous motor (PMSM) and its field-oriented control (FOC) are analyzed. Based on that, with the introduction of the dead-zone insertion method, the space vector pulse width modulation (SVPWM) mechanism is improved, and the PWM waveform that can realize the AC battery current is designed. A control strategy for regulating AC battery current to lock the battery temperature and avoid the battery voltage overrun is further designed. Secondly, the effectiveness of the model and the method was preliminarily verified by small-scale bench experiments. Through simulation, the precision, dynamic performance, and stability of the control strategy are verified compared with the original PMSM control algorithm. Finally, through the simulation under the China light vehicle test cycle (CLTC), the effect of the proposed method in real vehicle driving conditions is further evaluated. The contribution of this paper consists of (1) the proposed method that eliminates the necessity for altering the existing circuit topology or incorporating additional hardware in the BEV, and it remains compatible with the current PMSM FOC algorithm; (2) a novel mechanism that has been clearly identified for generating AC in the battery via the motor drive system while the vehicle is cruising; and (3) a unified computing platform that has been devised to integrate seamlessly the battery, motor, and controller, thereby enabling deeper insights into the battery self-heating mechanisms integrated with the motor drive system. This development paves the way for further exploration and refinement of the system's battery thermal management capabilities.

2. Material and Methods

2.1. The Introduction of Dead Zones

The FOC technology developed in the 1980s of the 20th century is now widely used in the control of PMSMs in BEVs. The hardware of a conventional three-phase PMSM inverter exhibits a three-phase full-bridge topology consisting of 6 power electronic devices. Power metal–oxide–silicon field-effect transistors (MOSFET) are employed, and the typical circuit topology is shown in Figure 1a. The three-phase stator windings of the motor are simplified to three inductors, A, B, and C, connected in a Y-type. The half-bridge consisting of two MOSFETs connected to each inductor is correspondingly called the A-phase, B-phase, and C-phase half-bridge. MOSFETs connected to the positive terminal of the power source are defined as upper tubes, which are represented as T_{AU}, T_{BU}, and T_{CU}, respectively, and the rest are called down tubes, which are represented as T_{AD}, T_{BD}, and T_{CD}, respectively. The power source has a voltage defined as V_{dc}.

The midpoint voltage V_i (i = A, B, C) of each half-bridge depends on the switching state of the MOSFETs, which constitute the half-bridge itself. The switch states are defined as S_i (i = A, B, C), assigned to 0 or 1, and their correspondence to midpoint voltage is shown in Table 1.

These different combinations of switch states form the basic voltage vector. The voltage vector shown in Figure 1b contains eight basic vectors consisting of 1 and 0, six of which are non-zero vectors or valid vectors: U_1~U_6, and two zero vectors: U_0 and U_7. Six non-zero vectors equitably divide an electrical period into six regions: I~VI in space. Through these eight basic vectors, spatial voltage vectors of any direction and size can be synthesized to form a rotating stator magnetic field. It is noteworthy that the time slice in which the upper and lower tubes are simultaneously turned off is defined as the dead zone, U_x, and is not included in the basic vectors.

In the FOC strategy, when the motor is in a driving condition, the direction of the bus current is always positive, and the battery is discharged. How to change the direction of the bus current and quickly charge and discharge the battery is the key issue to achieving battery AC self-heating. For this purpose, a dead zone is introduced to turn off the upper and down tubes of a phase simultaneously, and then the value of V_i is uncertain, which is opposite to the midpoint voltage of the basic vector before the dead zone. This makes it possible to reverse the direction of the bus current.

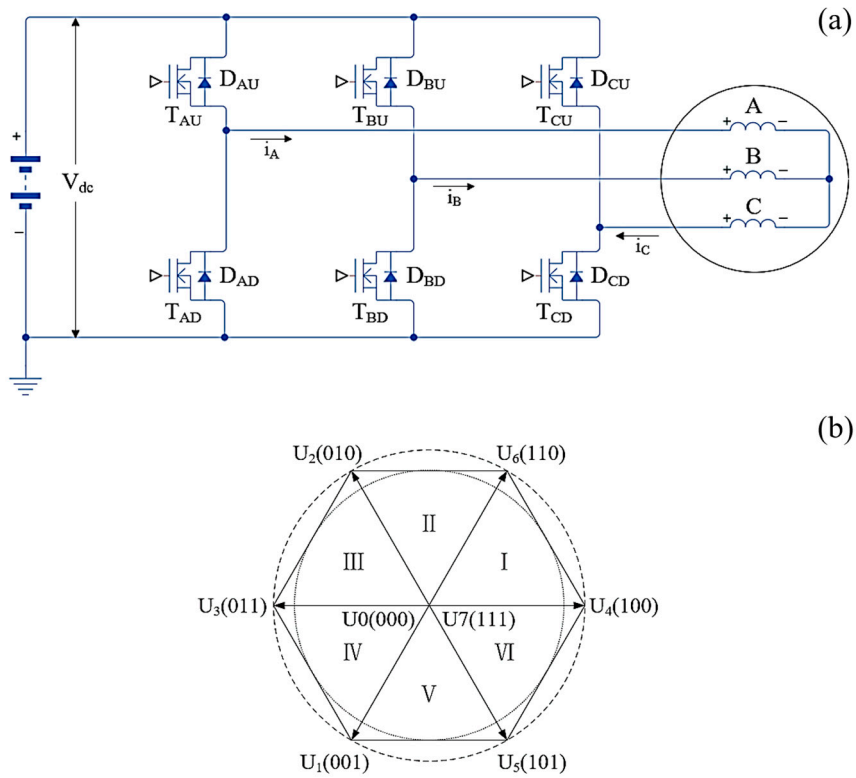

Figure 1. Principle of FOC of three-phase PMSM: (**a**) circuit topology of the inverter; (**b**) basic voltage vector diagram.

Table 1. Definition of switch states and their corresponding midpoint voltage.

State of T_{iU} *	State of T_{iD} *	Value of S_i *	Value of V_i *
ON	OFF	1	V_{dc}
OFF	ON	0	0
OFF	OFF	x	V_{dc} or 0

* Subscript character i represents A, B, or C.

2.2. The Effect of Dead Zones

Taking the vector U_4 as an example, the determining principle of V_i in dead zones and bus current is illustrated, as shown in Figure 2.

When T_{AU} is on, V_A is equal to $V_{dc} - V_{sw}$, where V_{sw} is the on-voltage drop of the MOSFET. Since T_{BD} and T_{CD} are on and their upper MOSFETs are closed, V_B and V_C are V_{sw}. At this point, the current in phase A, i_A, increases continuously in the direction shown by the green dotted arrow in Figure 2a. The sum of i_B and i_C is equal to i_A, and i_A equals the battery current. If the inverter is switched to the dead zone at this time, a turn-off gating signal is sent to all of the MOSFETs. The current in T_{AU} gradually decreases during its device storage time, and the corresponding current is transferred to the body diode D_{AD} at the down tube of phase A because i_A needs to be maintained. The voltage across T_{AU} rises, and the voltage across the diode D_{AD} drops to its on-voltage V_d. Thus, V_A is reduced to $-V_d$. Similarly, since the MOSFETs are all off, the current in T_{BD} and T_{CD} will also be transferred to the corresponding body diodes. The direction of the three-phase current is shown by the orange dashed arrow in Figure 2b. The current of phase A during the dead zone, i_A', is equal to the battery current. It can be seen that switching from a non-zero vector to a dead zone can realize the commutation of the battery current. In general, when the non-zero vector switches to the dead zone, the battery current reverses, the midpoint voltages Vi is transformed into the opposite of the original value, and the motor phase voltages are also

inverse. Similarly, when switching from a dead zone to one of the non-zero vectors, the conclusion is the same.

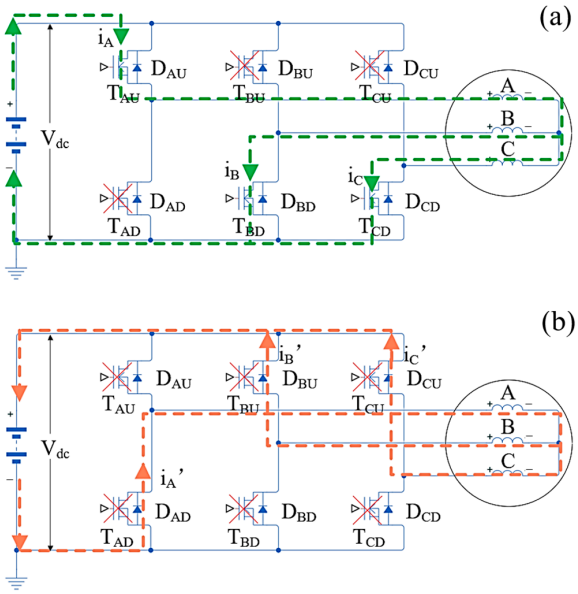

Figure 2. Schematic of the reverse current in FOC: (**a**) the current of each phase at vector U1; (**b**) the current of each phase in the dead zone.

The presence of a DC-link capacitor will weaken the amplitude of AC current, especially when the heating frequency is close to the resonance point of the resistor and inductor paralleled with the capacitor (RL-C) of the DC-link capacitor and motor stator circuit. Details can be referenced in the author's previous early-access article [28]. However, this situation can be avoided in application, and thus, the impact of the DC-link capacitor can be ignored. Therefore, if the influence of the DC-link capacitance is not considered, the correspondence between the bus current i_{bat} and the phase current can be referred to in Table 2. The battery current is equal to the inverter bus current, which is directly related to the heating power of the battery. Then, the state of charge (SOC) of the battery can be further calculated.

Table 2. The correspondence between the bus current i_{bat} and the phase current i_i (i = A, B, C) during different vectors.

Vectors	S_A	S_B	S_C	i_{bat}
U_4	1	0	0	i_A
U_6	1	1	0	$-i_C$
U_2	0	1	0	i_B
U_3	0	1	1	$-i_A$
U_1	0	0	1	i_C
U_5	1	0	1	$-i_B$
U_{nX} *	x	x	x	$-\max(\lvert i_i \rvert)$ *

* Subscript character i represents A, B, and C, and n represents 1~6.

Table 2 manifests that the magnitude of the bus current during the dead zone depends on the three-phase current of the previous non-zero vector and is numerically equal to the opposite of the largest absolute values in the three-phase current.

From the vector diagram in Figure 1b, the dead zone after each non-zero vector is the same as the vector with a phase difference of 180° from the non-zero vector itself. However, the switch combination is completely different. Under the condition of equal

magnitude transformation, the base vector in the vector diagram is determined by the following equation:

$$\mathbf{V}_{out} = \frac{2}{3}V_{dc}\left(s_A + s_B e^{j\frac{2\pi}{3}} + s_C e^{j-\frac{2\pi}{3}}\right) \quad (1)$$

Thus, the dead-zone vector corresponding to the base vector i can be expressed as:

$$\mathbf{V}_{out\,nX} = \mathbf{V}_{out\,n} e^{j\pi} (n = 1 \sim 6) \quad (2)$$

It can be seen that the output voltage vector $\mathbf{V}_{out\,nX}$ of any dead zone can always find a non-zero vector $\mathbf{V}_{out\,n}$, rendering the modulo of the two equal and the phase difference 180°. In the real FOC algorithm, the time control of the dead zone is particularly important. If the dead zone is too long, the current shown in Figure 2b will eventually decay to 0, all body diodes will be off, and the output voltage vector of the dead zone will no longer be equal to the reverse vector of the last vector but will be equivalent to the zero vector. When the zero vector is applied, the phase voltage and line voltage of the motor are all zero, so the phase current decays rapidly with time. The action time of the zero vector is uncertain in FOC and is related to the PWM period and output power. Although the zero vector cannot realize the commutation of the bus current, it is of great significance in regulating the heating power inside the battery.

2.3. Heating Intensity Adjustment Mechanism

To synthesize a space-rotating magnetic field, the SVPWM algorithm is used. The theoretical basis of the SVPWM algorithm is the principle of mean equivalence. That is, within a PWM period T_s, the basic voltage vectors are arranged so that their average value is equal to the given voltage vector. The output voltage vector synthesis, considering the dead zone, still needs to comply with the above principle in the natural coordinate system. Taking region I as an example, at some point, the output voltage vector $\mathbf{V}_{out}$ is synthesized by U_4' and U_6' in the direction of two non-zero base vectors of that region. To form the alternating current, the corresponding dead-zone vectors U_{4X} and U_{6X} are introduced, as shown by the red arrows in Figure 3. Since the dead-zone vector is inverse to its corresponding base vector, it is equivalent to reducing the magnitude of the original base vector. Therefore, in order to ensure the magnitude of the output voltage vector, the compensation vectors U_{4c} and U_{6c} should be introduced, which have the same direction as their base vectors.

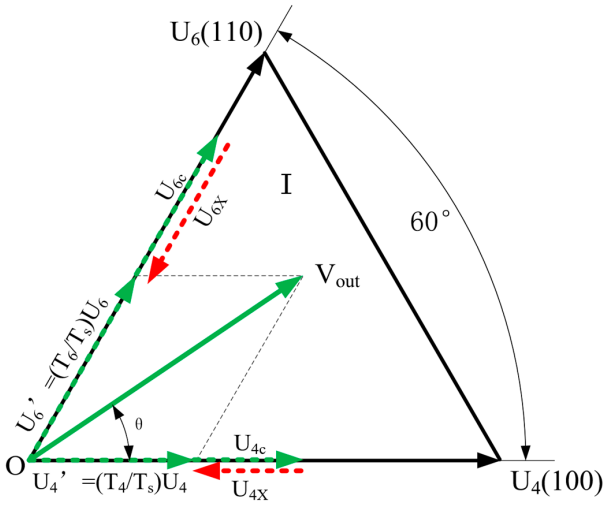

Figure 3. A spatial vector composition method with dead zones.

From the figure above, the compensation vector and the dead-zone vector seem to cancel each other geometrically and do not affect the direction and magnitude of the output voltage vector. Both the compensation vector and the dead-zone vector need to occupy

the action time of SVPWM, which will affect the magnitude of the output voltage vector. From this point of view, the superposition of the dead-zone vector and the compensation vector has the same effect on the output voltage vector as the zero vector. Therefore, this paper intends to modify the conventional SVPWM algorithm to replace part of the zero vector with a dead-zone vector and a compensation vector, hereinafter referred to as the dead-zone space vector pulse width modulation (dSVPWM) algorithm. According to the above analysis, the dSVPWM algorithm needs to meet the following equations:

$$T_s\mathbf{V_{out}} = T_4\mathbf{U_4} + T_6\mathbf{U_6} \tag{3}$$

$$T_s = T_4 + T_6 + T_0 \tag{4}$$

$$T_0 = T_0' + T_{4X} + T_{6X} + T_{4c} + T_{6c} \tag{5}$$

where T_0 represents the action time of the zero vector in the SVPWM algorithm, and T_0' represents the zero vector retained by dSVPWM. T_4 and T_6 represent the action time of non-zero base vectors U_4 and U_6, T_{4X} and T_{6X} represent the action time of the dead-zone vectors U_{4X} and U_{6X} in the dSVPWM algorithm, and T_{4c} and T_{6c} represent the action time of the compensation vectors U_{4c} and U_{6c}, respectively. Theoretically, T_{4X} equals T_{4c}, and T_{6X} equals T_{6c}. However, considering the nonlinearity of the circuit components, the compensation time needs to be adjusted appropriately. The ratio of the compensation time and dead time is defined as a_{cX}, hereinafter referred to as the compensation coefficient, and its expression is as follows:

$$a_{cx} = \frac{T_{6c}}{T_{6X}} = \frac{T_{4c}}{T_{4X}} \tag{6}$$

The compensation coefficient a_{cX} should be set to around 1; otherwise, the magnitude of U_4' and U_6' will be changed. In practice, calibration experiments for a_{cX} can be performed according to the phase current waveform. The ratio of T_{4X} and T_{6X} does not theoretically affect the output voltage vector. So, to make the equations have a unique solution, the following equation is specified:

$$\frac{T_{4X}}{T_{6X}} = \frac{T_4}{T_6} \tag{7}$$

In addition, define the ratio of time containing the dead zone and the compensation vector to the time of the original zero vector as heating intensity with the symbol b_n:

$$b_n = \frac{T_0 - T_0'}{T_0} = \frac{T_{4x} + T_{6x} + T_{4c} + T_{6c}}{T_0' + T_{4x} + T_{6x} + T_{4c} + T_{6c}} \tag{8}$$

The value of b_n indicates the time proportion of the AC production composed of the dead zone and its compensation vector. It can be predicted that the larger the b_n, the greater the AC of the battery. Therefore, the intensity of battery AC self-heating can be controlled by adjusting b_n.

So far, by inputting the magnitude V_{out} and direction θ of any target voltage vector and fixing the values of a_{cX} and b_n, T_4 and T_6 can be calculated according to Equations (9)–(11) and then the action time of each dead-zone vector and compensation vector can be obtained according to Equations (4)–(8).

$$T_4 = \frac{V_{out}T_s}{U_4}\left(\cos\theta - \frac{\sqrt{3}}{3}\sin\theta\right) \tag{9}$$

$$T_6 = \frac{2\sqrt{3}}{3}\frac{V_{out}T_s}{U_6}\sin\theta \tag{10}$$

$$U_4 = U_6 = \frac{2}{3}V_{dc} \tag{11}$$

The physical interpretation can be obtained by multiplying each solved time by the corresponding vector, which means that the volt-second area obtained by the output voltage vector $\mathbf{V}_{out}$ acting on one PWM period Ts can be obtained by summing the base vectors U_4' and U_6', the dead-zone vectors U_{4X} and U_{6X}, and the compensation vectors U_{4c} and U_{6c} multiplying with their corresponding action times. The magnitude of these vectors and their action time can be converted into a time series of switching the MOSFETs, which form corresponding PWM waves. The calculation method of the action time in other sectors is the same as in sector I.

The modulation ratio of dSVPWM is defined as:

$$M = \frac{\sqrt{3}|\mathbf{V}_{out}|}{V_{dc}} \tag{12}$$

To ensure that the composition vector is inside the linear region of a regular hexagonal, as shown in Figure 1b, the maximum magnitude of the output voltage vector $\mathbf{V}_{out}$ must be satisfied by $|\mathbf{V}_{out}| \leq 2V_{dc}/3$, while dSVPWM does not insert new non-zero vectors during each PWM period. Therefore, the maximum modulation ratio can still be 1.1547, which is consistent with the SVPWM algorithm.

After obtaining the action time of each vector, as long as the wave order is determined, the waveform of dSVPWM can be plotted. In this paper, a PWM scheme, as shown in Figure 4, is designed. Considering the adjustability for the time of the dead-zone vector, part of the zero vector is retained. To reduce the current ripple, a double-pulse mode is used per cycle. Each non-zero vector is divided equally into two parts and placed separately in each half period to maintain the symmetrical waveform pattern, thereby effectively reducing the harmonic component of PWM. From the analysis of Figure 4, it can also be known that the battery current alternates between positive and negative within a PWM cycle: during the non-zero vector action time slice, the battery current is negative, and the battery discharges; during the dead-zone slice, the battery current is positive, and the battery charges. Therefore, the period of the battery AC must be consistent with the PWM period. It is unrelated to the period of the phase current and the poles of the motor. This phenomenon will also be illustrated with an example in Section 4.2.2.

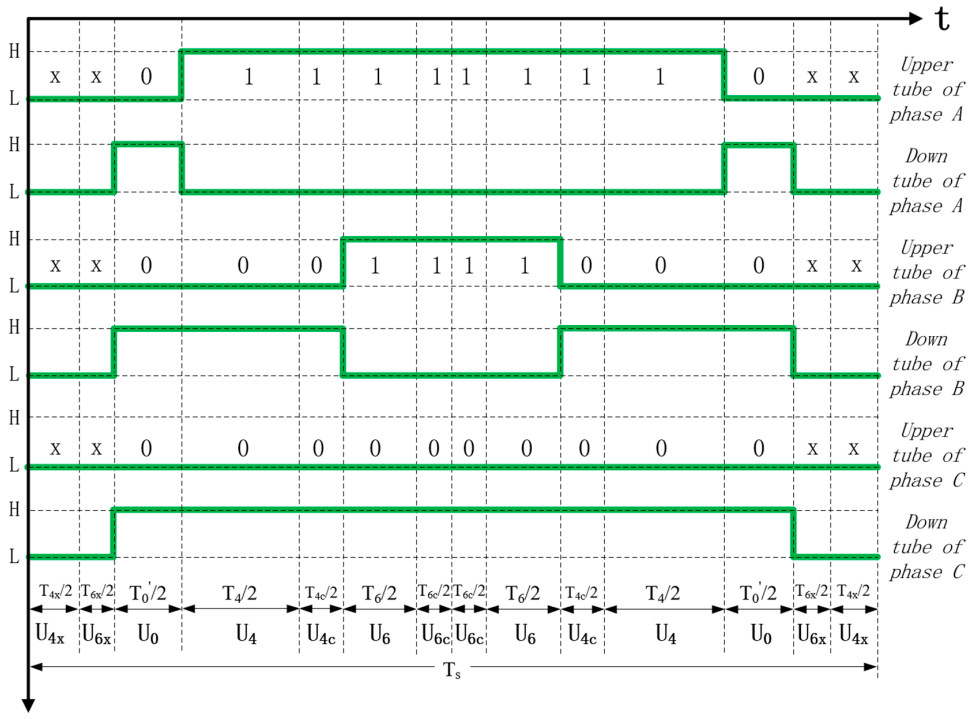

Figure 4. Switching waveform and vector composition of dSVPWM in one period.

To reduce the times of switching, each dead-zone vector and the compensation vector are also split in half so that the dead-zone vector is located at both ends to maintain the symmetry of the waveform and minimize the times of switching action. Each time toggling from a zero vector to a dead-zone vector, 3 MOSFETs need to turn off, and toggling from a dead-zone vector to a zero vector requires 3 MOSFETs to turn on. Therefore, the times of MOSFET switching per cycle is 14. Compared with the 12 times of the SVPWM algorithm based on the software mode, this is an increase of 2 times. For MOSFET inverters, switching losses are not the main source of power loss, and the small increase in the times of switching does not have much effect.

The general equation of battery heating power can be obtained from Joule's law:

$$P_{bat} = i_{bat\_s}^2 R_{bat} \tag{13}$$

where R_{bat} represents the equivalent ohmic internal resistance of the battery, P_{bat} represents the battery heating power, and i_{bat_s} represents the root-mean-square value of the battery current in one FOC period. According to the dSVPWM algorithm proposed above, taking region I as an example, when $i_A > 0$, $i_B < 0$, and $i_C < 0$, the quadratic of the i_{bat_s} can be expressed as:

$$i_{bat\_s}^2 = \frac{1}{T_s}\left(\int_0^{(T_4+T_{4c})/2} i_A^2 dt + \int_0^{T_6+T_{6c}} i_C^2 dt + \int_0^{(T_4+T_{4c})/2} i_A^2 dt + \int_0^{T_{4X}+T_{6X}} i_A^2 dt\right) \tag{14}$$

From Equation (14), it can be seen that the battery heating power is not only related to the value of the motor phase current but also related to its action time in a FOC period. It is noteworthy that in the traditional SVPWM scheme, the battery current is zero when the zero vector is applied, while in the proposed dSVPWM algorithm, in the primordial zero vector action time, an alternating battery current is formed, which effectively improves the battery heating power. Moreover, under the action of the dead-zone vector, the absolute value of the battery current always takes the maximum value of the three-phase current, as shown in Table 2, thus further increasing the battery heating power.

On the other hand, the proposed dSVPWM changes the ripple of the phase current, which directly determines the electromagnetic force of the motor. This will inevitably produce high-frequency torque fluctuations on the motor output shaft and may form high-frequency noise. The torque fluctuations will be discussed in Section 4.2.5 in the following text, while NVH is not the focus of this paper and will be analyzed in subsequent research.

2.4. Small-Scale Motor Driving System Test Bench

A small-scale motor driving system test bench, as shown in Figure 5, was built to verify the feasibility and advantages of the above heating strategy. The battery pack was assembled by 12 cells (INR18650/25P, EVE Energy Co., Ltd., Huizhou, China) connected in series. Its rated voltage is 43.2 V, and the maximum discharge rate is 10 C. The battery pack was fully charged to 2.5 Ah at room temperature and discharged to a SOC of 60%. The surface of the battery pack was not insulated and was in natural convection with the ambient air. The terminals of the battery pack were connected to the homemade driver board through the direct current (DC) link, and two wires were connected to the control board to accurately measure the terminal voltage of the battery pack. The DC-link currents and battery voltages were monitored and recorded by an oscilloscope (DSO2014A, Keysight, Santa Rosa, CA, USA) during the test. The motor used in the test is a PMSM for an electric tricycle with a rated power of 1 kW. Its detailed parameters are shown in Table 3. These parameters are provided by the vehicle manufacturer. The motor was mounted on a 2 kW electromagnetic dynamometer (ZD10, Guangzhong Electrical Equipment Co., Ltd., Taizhou, China). Forced air cooling was adopted for the controller and inverter by a fan to prevent overheating. The motor was cooled by natural convection at room temperature. A digital signal processor (DSP) is embedded in the control board, which is used to run the control strategy designed in this paper.

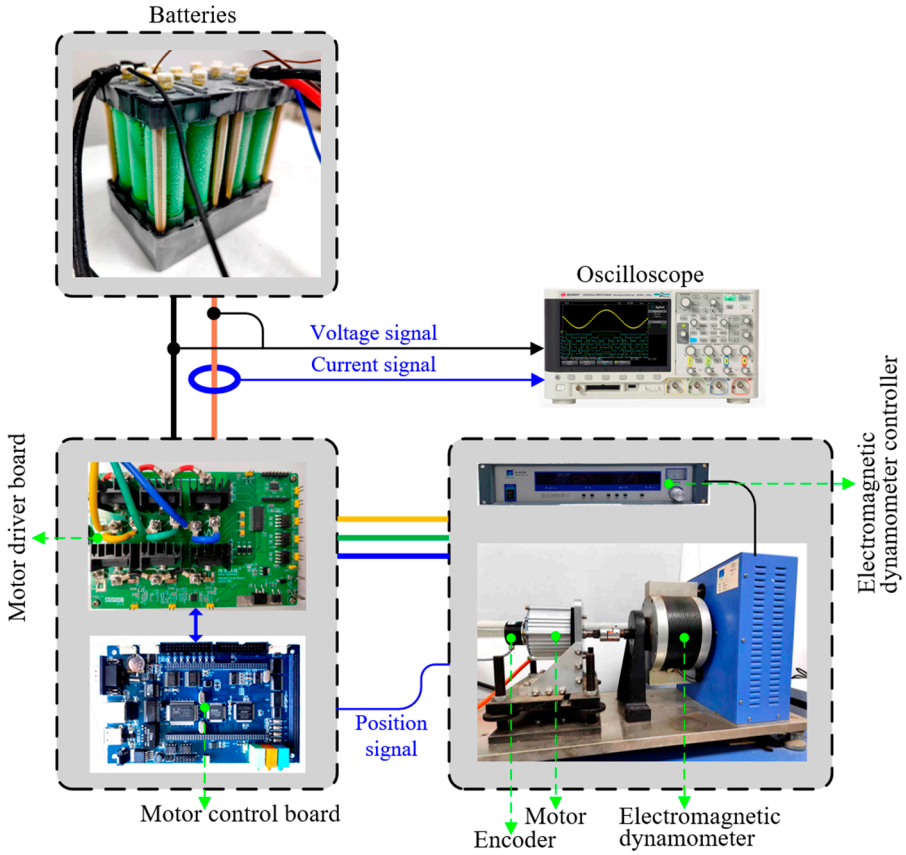

Figure 5. Small-scale motor driving system test bench.

Table 3. Parameters of the motor in the test.

Parameters	Value	Unit
Rated current	27	A
Rated voltage	48	V
Inductance of d-axis	71.2	uH
Inductance of q-axis	99.5	uH
Phase resistance	15.1	mΩ
Pole pairs	5	-
Flux linkage	1.67×10^{-2}	Wb
Back EMF constant	15.4	V/krpm
Rotational inertia	1.90×10^{-4}	kg·m^2
Friction coefficient	3.20×10^{-3}	N·m·s

3. Simulation and Calculation

3.1. Small-Scale System Models for Experimental Validation

To verify whether the dSVPWM algorithm can be used in the FOC control strategy of PMSM and realize AC heating of the battery while driving, based on the algorithm described in Section 2, the physical model of the small-scale motor driving system test bench is built in Simulink to carry out the numerical calculation. The parameters used in the model are the same as those on the test bench. The battery is programmed by Matlab function as a fractional order equivalent circuit model, and its parameters are measured by the electrochemical workstation (CS1350, Corrtest Instruments Co., Ltd., Wuhan, China). Firstly, the precision of the model is verified by comparing it with the small-scale test bench, and then the characteristics of the proposed algorithm are studied by comparing the dSVPWM algorithm with the original SVPWM algorithm. The model adopts a closed-loop structure with a dual PI of current and speed. The PI loop for current employs internal

mode control for PI parameter tuning [29]. PI parameter tuning of the speed loop is based on the active damping method proposed in the literature [30]. The completed model is shown in Figure 6. The blue shading module contains the dSVPWM algorithm. The green shading module is the original SVPWM algorithm for comparative studies. The controller in the model adopts the basic FOC method, id = 0 control, and the parameters used are shown in Table 4.

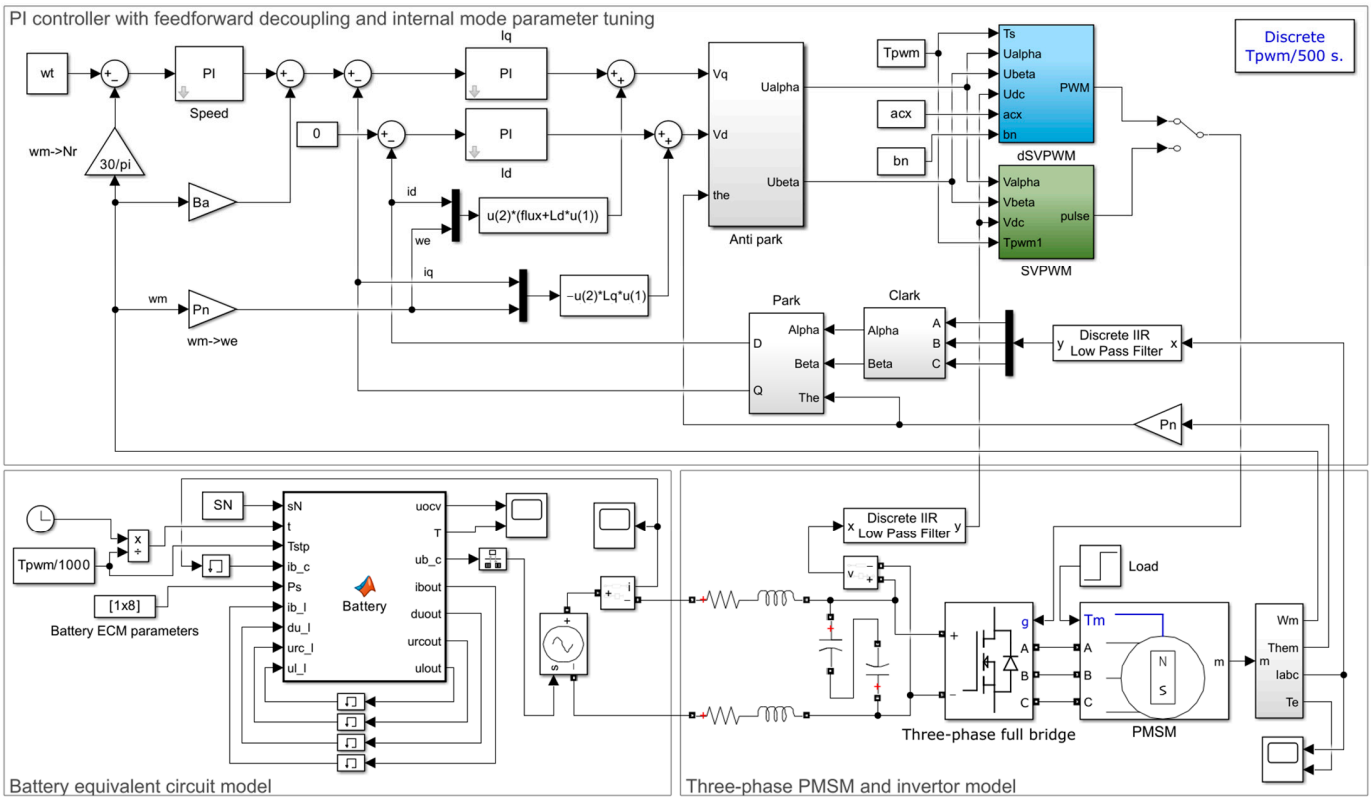

Figure 6. Powertrain models of a BEV in Simulink.

Table 4. Parameters of the controller in the model.

Parameters	Value	Unit
Proportional gain for d-axial current loop	3.56×10^{-2}	-
Integral gain for d-axial current loop	7.55	-
Proportional gain for q-axial current loop	4.98×10^{-2}	-
Integral gain for q-axial current loop	7.55	-
Proportional gain for speed loop	7.6×10^{-2}	-
Integral gain for speed loop	3.8	-
PWM period	1×10^{-4}	s
PI controller period	1×10^{-3}	s
Bandwidth for speed loop	50	rad/s
Bandwidth for the current loop	2500	rad/s

3.2. Vehicle-Level Powertrain Model and Parameters

In order to verify the proposed method for locking battery temperature while driving at the vehicle level, the parameters in the model shown in Figure 6 are refreshed according to the motor and battery pack parameters of a pure electric passenger car reported in the literature [27]. The main parameters used in the vehicle-level model are shown in Tables 5 and 6.

Table 5. Parameters of the motor in the vehicle-level model.

Parameters	Value	Unit
Peak power	160	kW
Rated voltage	354	V
Inductance of d-axis	0.09	mH
Inductance of q-axis	0.24	mH
Phase resistance	5	mΩ
Pole pairs	4	-
Flux linkage	0.036	Wb

Table 6. Parameters of the battery pack in the vehicle-level model.

Parameters	Value	Unit
Initial temperature	−10	°C
Ambient temperature	−35	°C
Initial SOC	65	%
Serial number	90	s
Rated voltage	324	V
Nominal capacity	100	Ah
DC-link Equivalent resistance	0.5	mΩ
DC-link Equivalent inductance	8	μH
Specific heat capacity	935	$J \cdot kg^{-1} \cdot K^{-1}$
Surface heat transfer coefficient	10	$W \cdot m^{-2} \cdot K^{-1}$
Thermal conductivity in axial	15.1	$W \cdot m^{-1} \cdot K^{-1}$
Thermal conductivity in radial	0.45	$W \cdot m^{-1} \cdot K^{-1}$

The equivalent circuit model of the cell remains the same as the model described in Section 3.1, and after the cell is properly connected in series and parallel, the voltage and capacity required for the motor in Table 5 are obtained. In addition, the lumped-parameter heat transfer model of the cell is added here to calculate the temperature rise of the battery. The heating power of the cell is calculated by Equation (14). The thermophysical parameters are listed in Table 6.

The ambient temperature in the model was set to −35 °C to simulate extreme cold weather. The initial battery temperature is set to −10 °C, which represents the battery temperature of the vehicle after it has been warmed up during parking.

In the above Simulink model, let the motor run following the CLTC speed; meanwhile, calculate the battery voltage, current, temperature, and other parameters, which are used to evaluate whether the proposed temperature locking strategy can work in real operation of the vehicle, when it works, and how effective it is.

For this purpose, the speed of the vehicle's motor under CLTC and the corresponding load torque must be obtained. According to the longitudinal dynamic equation of the vehicle, the relationship between the driving force and the vehicle speed can be expressed as:

$$F_t = \delta m \frac{dv}{dt} + f_0 + f_1 v + f_2 v^2 \quad (15)$$

In the equation, F_t represents the driving force. m is the vehicle test mass. δ is the rotational mass conversion coefficient. v represents the vehicle speed. f_0 and f_1 are the rolling resistance coefficients. f_2 is the coefficient related to wind resistance, which can be calculated as $C_D \cdot A \cdot v^2/21.15$, where C_D is the vehicle's coefficient of air resistance and A is the windward area.

Combined with the parameters provided by a vehicle manufacturer, as shown in Table 7, the vehicle speed in the CLTC diagram can be converted into the speed of the motor, and the driving force can be calculated according to Equation (15), and the motor load torque can be further obtained. This paper only focuses on the data from 274 to 520 s in CLTC, which represents the characteristics of urban scenarios, such as low-speed

driving, stop-and-go, etc. The vehicle speed before and after this period is much higher, and the battery temperature then has been verified as not dropping in simulation. The heat dissipation condition of the battery is set to natural convection with air. If the vehicle is driving, the heat dissipation conditions of the battery will be better, which means that the battery temperature drops more easily. Of course, the battery pack in BEVs now commonly uses liquid cooling or direct refrigerant cooling methods, in which the heat transfer process between the battery and the cooling medium is forced convection, and the heat exchange efficiency is much higher than that of natural convection. Therefore, the simulation conditions in this paper are relatively demanding, and the results must be more convincing.

Table 7. Parameters for calculating motor speed and torque from CLTC.

Parameters	Value	Unit
Vehicle test mass	1990	kg
Tire radius	0.3588	m
Rolling resistance coefficient f_0	133	-
Rolling resistance coefficient f_1	1.097	-
Coefficient f_2	0.041	-
Rotational mass conversion coefficient	1.018	-

The calculated motor speed and torque are shown in Figure 7. Obviously, vehicle speed is less than 20 km/h in the selected period, which includes three driving–stopping cycles: driving for 17 s then stopping for 35 s, driving for 26 s then parking for 50 s, and driving for 35 s then parking for 85 s. Acceleration and deceleration in the first two cycles are greater than those in the third one. This characteristic represents typical Chinese urban road conditions.

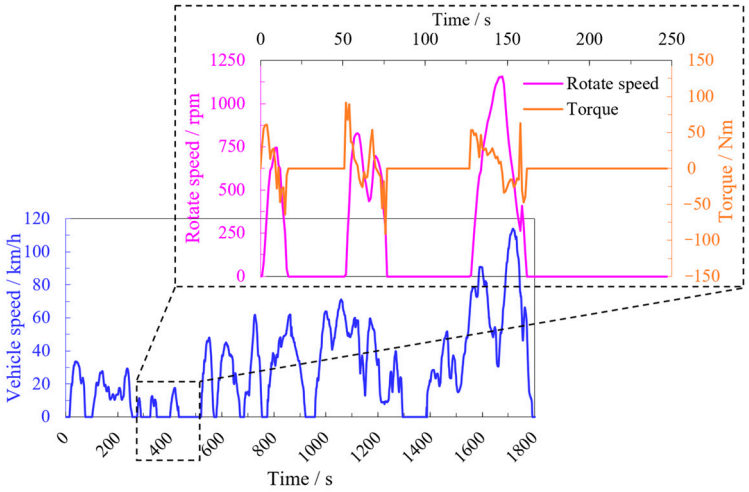

Figure 7. Motor speed and load torque calculated according to the low-speed period of CLTC.

3.3. Structure and Workflow of Hysteresis Control for Battery Temperature

Based on the proposed dSVPWM algorithm, this paper proposes a temperature-locking strategy for power batteries during vehicle driving, which employs hysteresis control to maintain the temperature of the battery within the set upper and lower thresholds and prevent the occurrence of the vehicle speed limit or accidental breakdown caused by the drop in battery temperature during driving.

The main idea of this strategy is to automatically adjust the motor control strategy according to the feedback of battery temperature and change the self-heating power of the battery by updating the battery heating intensity b_n in real time so that the battery temperature is always maintained above the threshold. The structure of this control strategy is shown in Figure 8. The control period is the same as the PWM period. The

target temperature consists of a low threshold T_{bl} and a high threshold T_{bh}, the difference of which is the hysteresis band, which can be set to about 0.5 °C. In the model, T_{bl} and T_{bh} are set to −10.3 °C and −9.8 °C, respectively. When the average temperature of the battery is lower than T_{bl}, the dSVPWM algorithm is started, the battery heating intensity b_n is increased in increments of 2×10^{-4} per control period, and the change rate of the average temperature of the battery is monitored in real-time. If the change rate of battery temperature is still not inverted in the next control period, the heating intensity b_n will continue to increase until the average battery temperature begins to rise. If the battery temperature reaches a high threshold T_{bh}, the dSVPWM algorithm will exit and revert to the SVPWM algorithm.

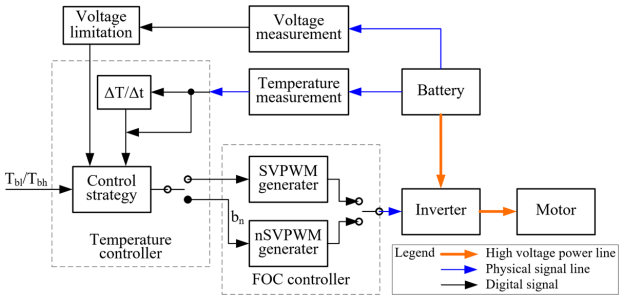

Figure 8. Control structure of hysteresis control for temperature locking during vehicle driving.

The algorithm flowchart is shown in Figure 9. In addition to the battery temperature control strategy, the figure also includes the control strategy for battery voltage. If the battery voltage is detected close to the upper or lower thresholds, the b_n quickly decreases by a speed of 2×10^{-3} per period to avoid voltage overruns due to the heating strategy. This is to avoid the battery terminal voltage exceeding its limited operating voltage at a large heating intensity when the battery SOC is high or low. If the battery voltage still exceeds the limit when the b_n is reduced to zero, the security measures of the BMS will be triggered, which is outside the scope of this paper.

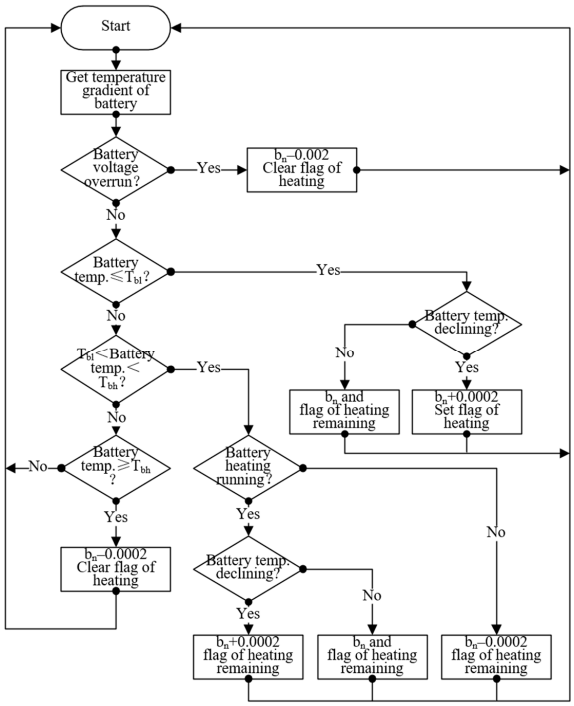

Figure 9. Flow chart of hysteresis control for temperature locking during vehicle driving.

4. Results and Discussion

4.1. Experimental Validation for Speed Control Based on dSVPWM

The model shown in Figure 6 was used to simulate the closed-loop control of the speed under fixed working conditions, and the synchronous comparison test was carried out on the small-scale electric drive system test bench shown in Figure 5. On the one hand, the effectiveness of the model structure and parameter was verified by the comparison test, and on the other hand, the advantages of the dSVPWM algorithm over the SVPWM algorithm in battery self-heating were also verified. These comparisons only concern battery current, as its amplitude and symmetry directly reflect the battery heating rate and effect. The initial temperature of the comparison test was maintained at a room temperature of 25 °C; the battery temperature was not measured, and only the battery current after stabilization was recorded. The motor was not loaded in the test, and it was found that the battery current amplitude was sufficient for comparison under no load, so the motor load torque in the model was also set to zero. The motor used in this test is designed for a low-speed vehicle, and its maximum speed is only 3000 r/min; therefore, three points of 500, 1000, and 1500 r/min were selected in the test, representing creep, low-speed, and medium-speed driving conditions, respectively. In high-speed driving, the output current of the battery is much larger, and its DC heating power is considered to be sufficient to resist the battery temperature drop while driving in a low-temperature environment, so the high-speed driving condition is not the focus of this study.

The simulation and experimental data of the battery current based on SVPWM at a speed of 500 r/min are shown in Figure 10. The numerals 1, 2, 3, and 4 depicted in the this figure and those that in the following text denote the channel designations of the oscilloscope, with the colors of these numerals matching the hues of the corresponding curves in the figure. From a macroscopic point of view, the positive and negative amplitudes of the battery current calculated by the model are basically the same as the experimental values. Microscopically, the experimental value has a harmonic wave of about 4 Hz, resulting in the battery current becoming unstable. The time scale of the harmonic period is much larger than the PWM period and the adjustment period of the PI controller, which is considered to be related to the mechanical characteristics of the motor shaft system. The simulation results also have harmonic components, mainly at a period of 1 ms, which is the same as the control period of the speed loop, so it is speculated that it is caused by the regulation of the speed loop PI controller. Battery current comparison data at speeds of 1000 and 1500 r/min is shown in Figures 11 and 12, respectively. On the whole, the increase in speed will cause the positive battery current to increase proportionally while the battery charge current does not increase significantly.

In order to observe the adjusted effect of the dSVPWM algorithm on battery heating intensity, the dead zone is added to the working conditions of 450 r/min. Comparison results between the dSVPWM algorithm, with b_n = 20% and 50%, and the original SVPWM algorithm, with b_n = 0, are shown in Figure 13. It can be seen that with the increase of b_n in the dSVPWM algorithm, an obvious charge current of the battery emerges, and the discharge current of the battery also increases significantly. In addition, the motor speed was quite stable during the experiment. This shows that the dSVPWM algorithm can superimpose a large AC on the battery's DC discharge current to realize the self-heating of the battery. More importantly, the amplitude of the superimposed AC can be adjusted by b_n to realize the adjustable and controllable heating intensity of the battery.

Through the above experimental data, the theoretical feasibility of the dSVPWM algorithm in motor speed control is preliminarily verified. Through the comparison of experimental and model calculation results, the accuracy of model structure and parameters is verified. The experimental data also prove the controllability of the dSVPWM algorithm on the battery AC. Based on this, the feasibility study on battery pack heating based on the dSVPWM algorithm will be further carried out in the following sections of the simulation.

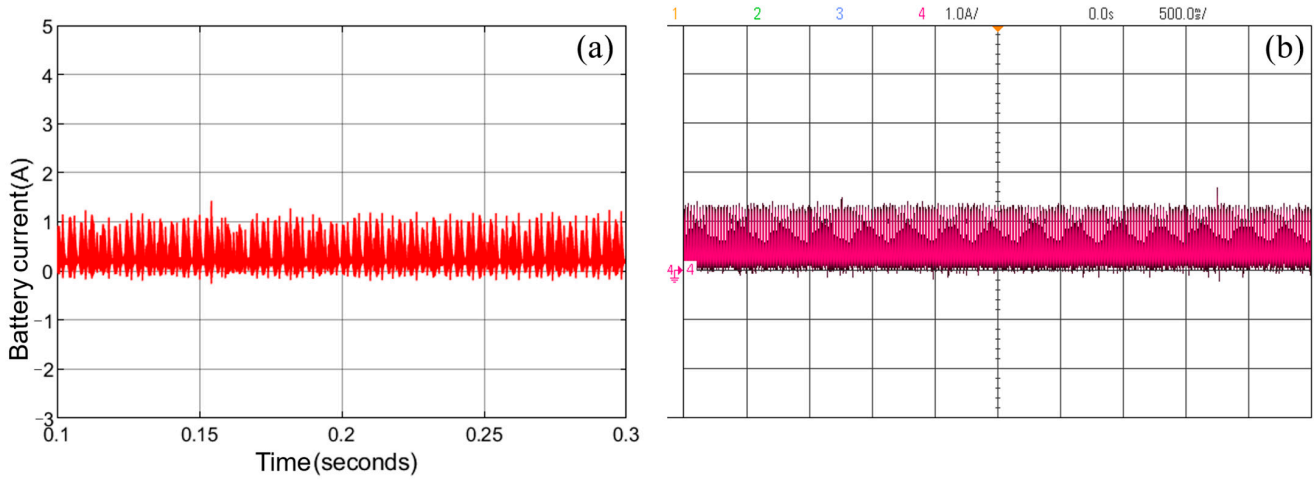

Figure 10. Comparison of the battery current calculated by the model and measured in the experiment based on SVPWM at a fixed speed of 500 r/min: (**a**) simulation data, (**b**) experimental data.

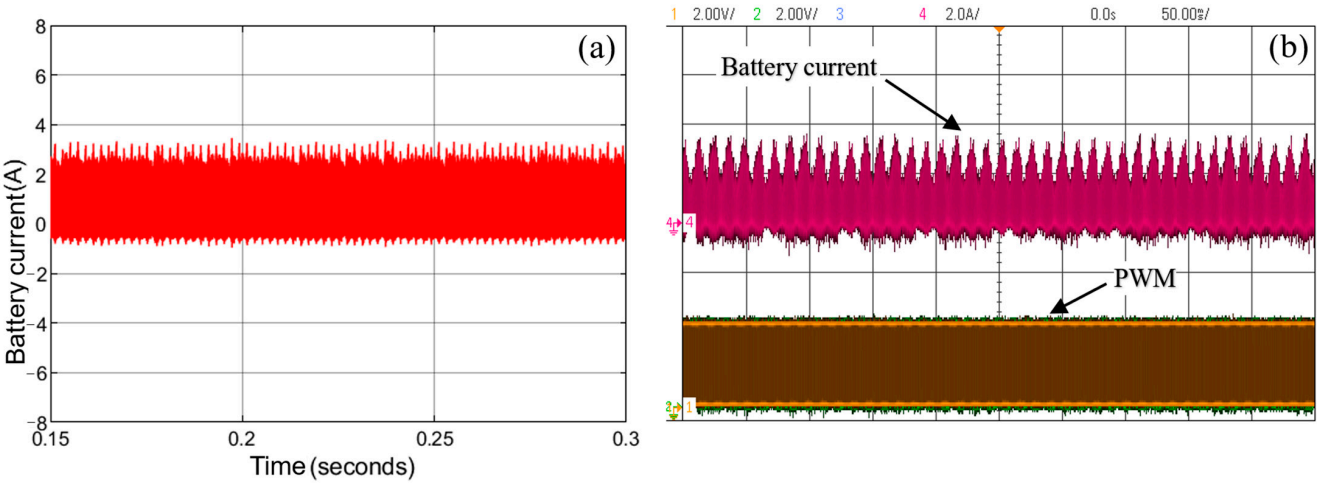

Figure 11. Comparison of the battery current calculated by the model and measured in the experiment based on SVPWM at a fixed speed of 1000 r/min: (**a**) simulation data, (**b**) experimental data.

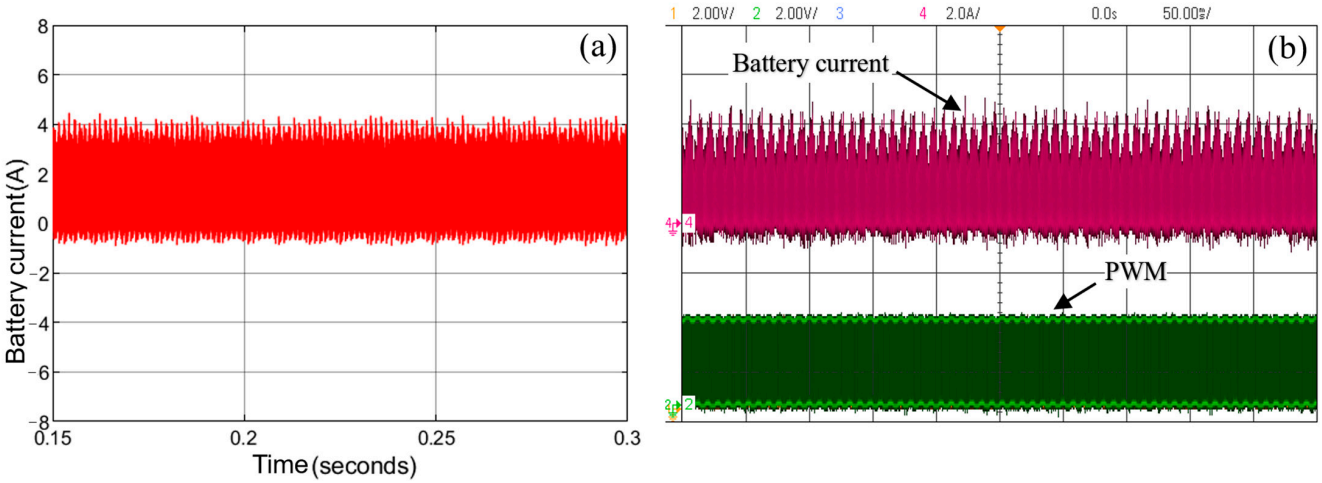

Figure 12. Comparison of the battery current calculated by the model and measured in the experiment based on SVPWM at a fixed speed of 1500 r/min: (**a**) simulation data, (**b**) experimental data.

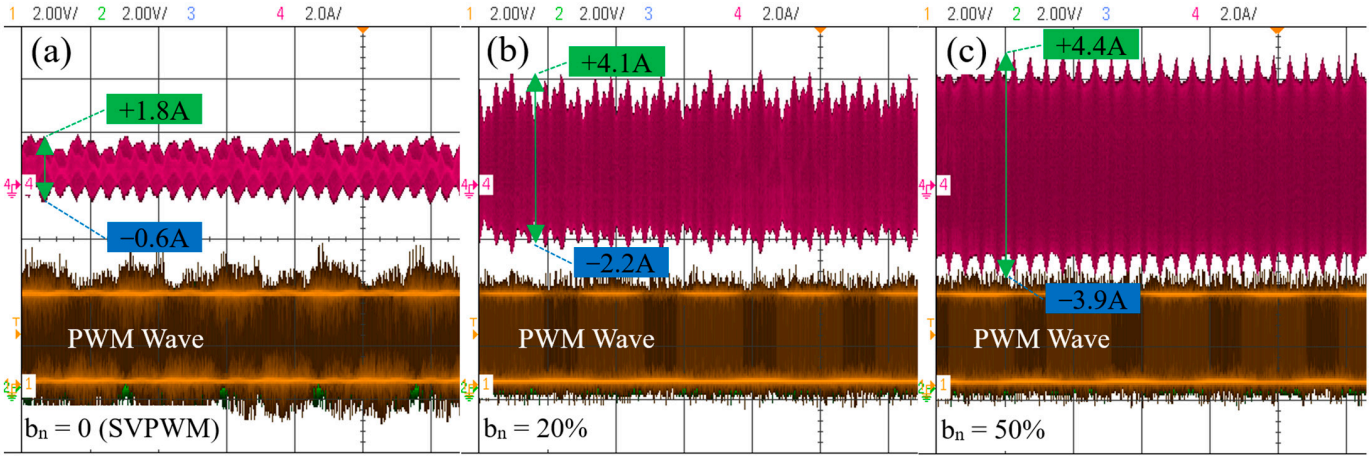

Figure 13. The effect of the dSVPWM algorithm on modifying the battery current in the experiment: (**a**) b_n = 0, (**b**) b_n = 20%, (**c**) b_n = 50%.

4.2. Comparison of dSVPWM and SVPWM Algorithm Using Simulation

4.2.1. Comparison of Motor Phase Current

The target speed was set to 2500 r/min, the motor load was set to a constant 1.0 Nm, and both b_n and a_{cx} were set to 1. The initial and ambient temperatures of the battery were set to 20 °C. The motor phase currents at 0.3 s for dSVPWM and SVPWM algorithms were recorded, respectively, as shown in Figure 14. At this time, the motor speed had been stabilized. The figure shows that there is no significant difference in the mean value of the phase current, while the peak current of the dSVPWM algorithm increases slightly, and its ripple is larger, especially near the peak. This is due to the commutation of the voltage vector caused by the switching of the non-zero vector and dead zone, and the voltage difference is almost twice that of SVPWM, so a larger ripple current is formed. In general, the sinusoidal fluctuation of the motor phase current can still be maintained in the dSVPWM algorithm, and its root-mean-square value and the phase difference have not changed significantly under the same working conditions.

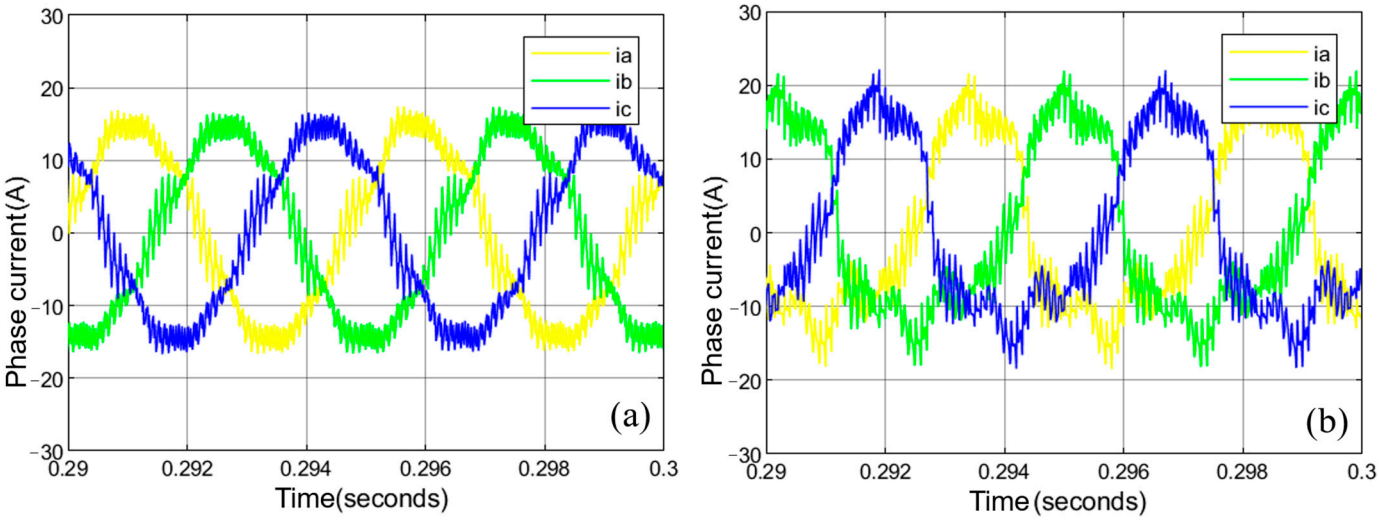

Figure 14. Comparison of motor phase current: (**a**) SVPWM algorithm, (**b**) dSVPWM algorithm.

4.2.2. Comparison of Battery Current

The comparison of battery currents under the same operating parameters as Section 4.2.1 is shown in Figure 15. Obviously, the control strategy using the SVPWM algorithm does not

form AC battery current, while the motor control strategy using the dSVPWM algorithm generates alternating currents in the battery, and the amplitude of the current is greatly increased. From Figure 15c, the local magnification of Figure 15b, around 0.3 s, it can be seen that the period of AC battery current coincides with the PWM period T_s and that the positive and negative peaks of the alternating current are not equal. The positive peak is greater than the negative peak, and the proportion of the positive and negative values of the alternating current in time is quite different, which is determined by the proportion of the dead zone in the dSVPWM algorithm. Especially in high-speed conditions, non-zero vector accounts for the majority of a PWM period, and the proportion of dead zone is quite small, so the time that negative current accounts for is less than positive current. In addition, similar to the phase current, the peak ripple of the dSVPWM algorithm is significantly higher than that of SVPWM for the same reason as above. Keeping the other operating parameters unchanged, the target speed was set to 500 r/min. This simulation result of the battery current is shown in Figure 15d, which shows that the amplitude of the alternating current at low speed has been greatly improved. This is because, at low speeds, the dSVPWM algorithm has a larger proportion of zero vectors, giving more time to generate AC without changing the b_n.

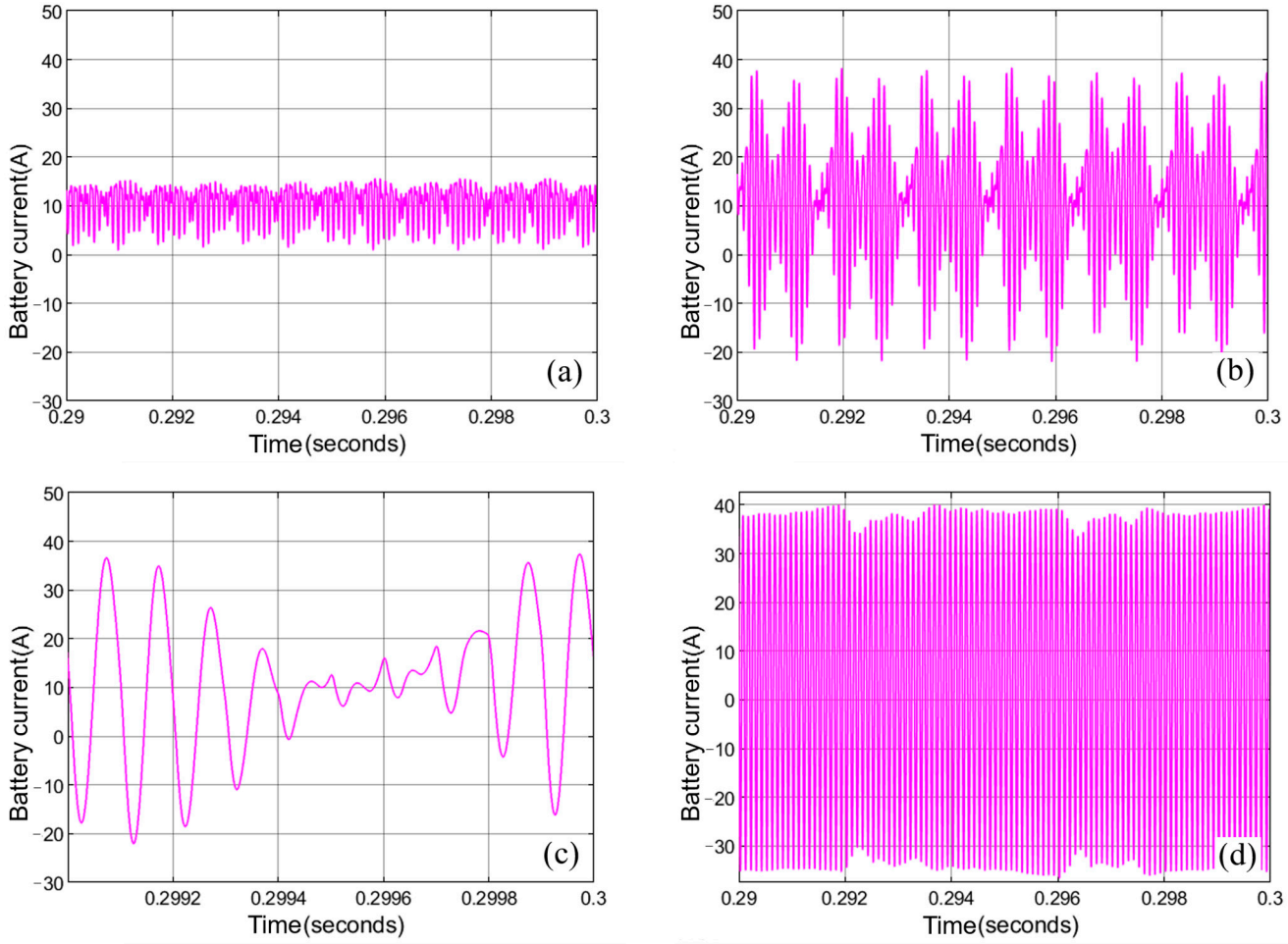

Figure 15. Comparison of battery current: (**a**) SVPWM algorithm, (**b**) dSVPWM algorithm at high speed, (**c**) local magnification of (**b**), (**d**) dSVPWM algorithm at low speed.

4.2.3. Comparison of Step Response to Torque Loads at Medium or High Speed

The torque of the motor was set to zero when the time was less than 0.15 s and increased to 1.0 Nm in step from 0.15 to 0.3 s, and the target speed was set to 2500 r/min. Under these conditions and keeping the others the same as in Section 4.2.1, the dynamic

process and stability of the two algorithms were compared under the conditions of no load and step load. The results of the simulation are shown in Figure 16, which shows that the two algorithms can remain stable under both no-load and constant-load conditions, and the speed error is zero. Compared with the SVPWM algorithm, the dSVPWM algorithm has a larger overshoot but a smaller rise time. In general, there is not much difference in dynamic performance.

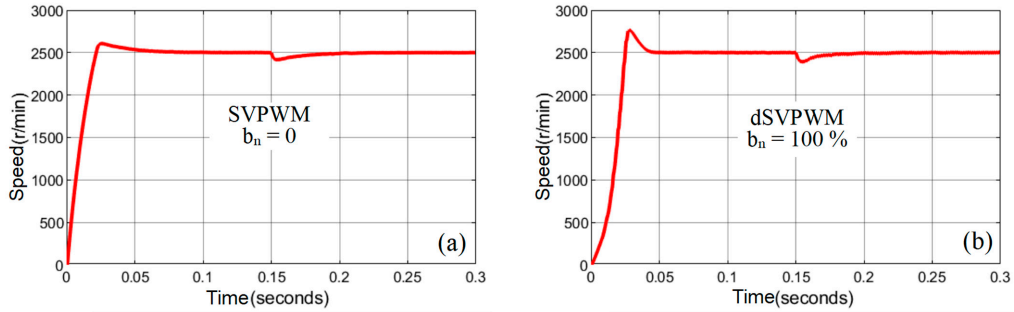

Figure 16. Step response to torque loads at medium or high speed: (**a**) SVPWM algorithm, (**b**) dSVPWM algorithm.

4.2.4. Stability of Speed Control at Low Speeds and Small Load

The target speed of the motor was set to 500 r/min, and the torque condition remained unchanged. The influence of the two algorithms on the speed control characteristics of the motor under low-speed conditions was studied, and the calculated speed figures are shown in Figure 17. Thereinto, Figure 17a–c indicate that the dSVPWM algorithm can control and maintain a stable speed at low speed and is not affected by the value of b_n, but the overshoot is higher than that of the SVPWM algorithm. In addition, compared with Figure 17d, they show that the overshoot of response to the torque disturbance using the dSVPWM algorithm is also larger. But in the end, both algorithms can overcome the torque disturbance and maintain the stability of the speed. In general, the dSVPWM algorithm does not affect the speed control of the motor at both high and low speeds.

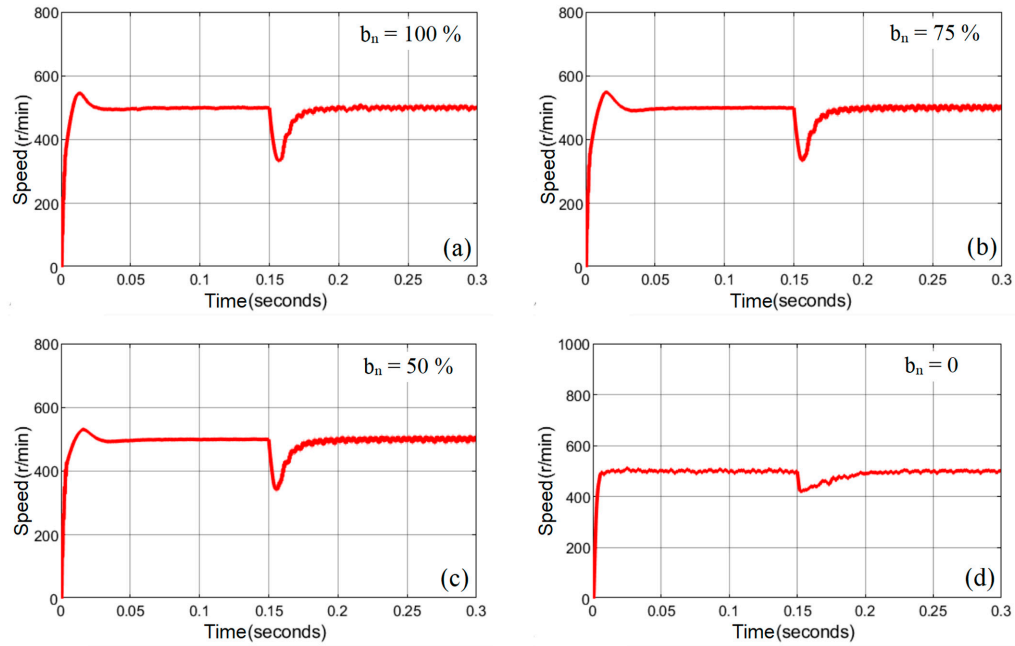

Figure 17. Step response to torque loads at low speed: (**a**–**c**) dSVPWM algorithm at different b_n, (**d**) SVPWM algorithm.

4.2.5. Comparison of Torque Fluctuations at Low Speed

The target speed of the motor was set to 500 r/min, and the torque condition remained unchanged. Take the simulation result of torque for the last 0.01 s, as shown in Figure 18, which shows that the average torque of the two algorithms is the same, while the torque of the dSVPWM algorithm produces a symmetrical ripple based on the SVPWM algorithm. The frequency of this ripple is the same as the PWM frequency, so it can be inferred that the torque fluctuation is due to the phase current ripple caused by the dead-zone vector. Further comparison of Figure 18a–c shows that the magnitude of the torque ripple decreases with the decrease of b_n, which further indicates that the ripple is caused by the dead zone added to the dSVPWM algorithm. Due to the high frequency and small amplitude of this torque ripple, 10 kHz and less than ±1 Nm, it is easily filtered by mechanical systems with large time constants. In addition, the simulation results show that with the increase in speed, the proportion of dead zone decreases, and the amplitude of the torque ripple will also decrease accordingly.

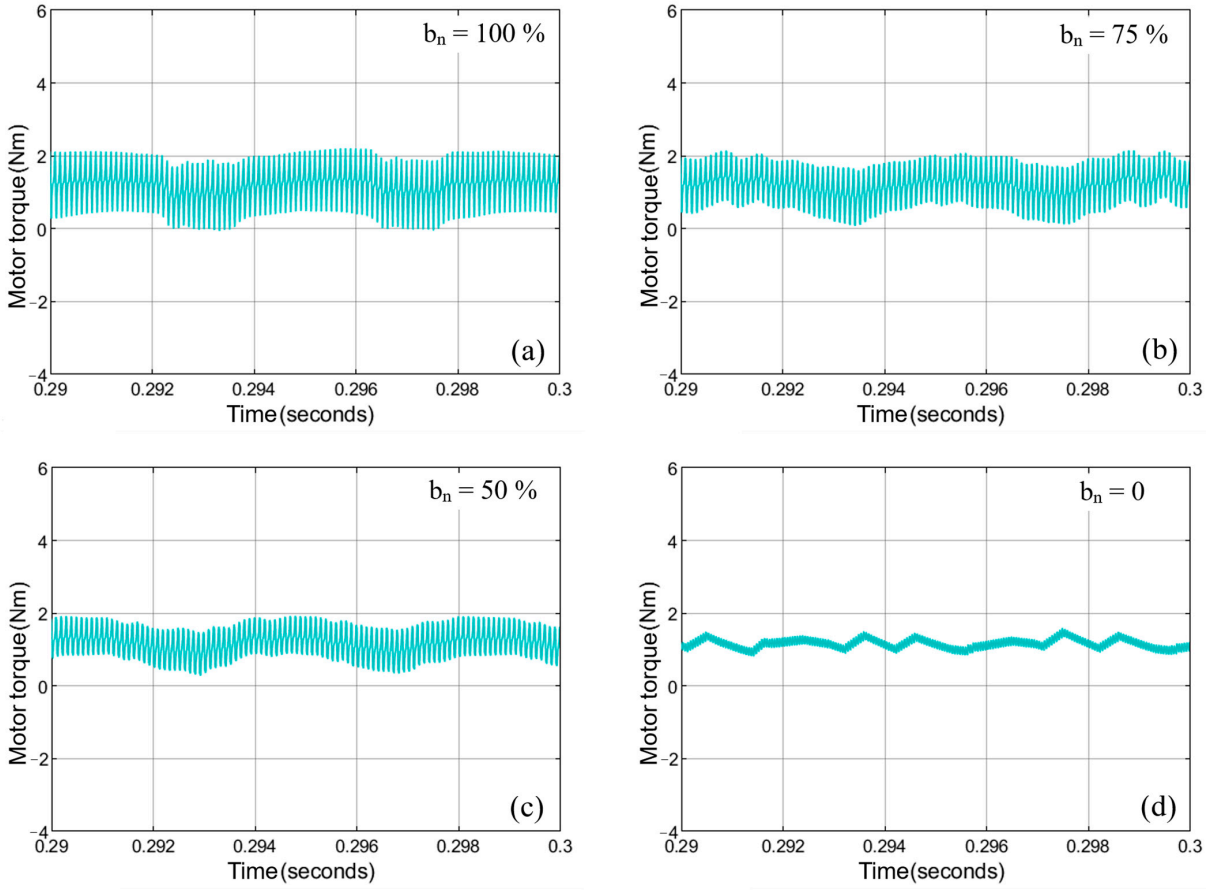

Figure 18. Motor torque ripple at low speed: (**a**–**c**) dSVPWM algorithm at different b_n, (**d**) SVPWM algorithm simulation results of temperature-locking strategy under CLTC driving conditions.

4.2.6. Simulation Results Related to Vehicle-Level Powertrain Model

The simulation results are shown in Figure 19, which includes (a) motor speed tracking accuracy; (b) peak and trough value per PWM cycle of battery voltage; (c) peak and trough value per PWM cycle of battery current; (d) heating intensity b_n and the comparison of the average battery temperature with or without temperature-locking strategy. Figure 19a explicitly shows that the motor can track the target speed under CLTC conditions well, and the speed is almost error-free, without overshoot and jitter. As can be seen from Figure 19b, the battery current has a large amplitude during driving, but it is unstable and changes drastically with the load. Especially during the rapid acceleration and deceleration of the

vehicle, there are several large spikes. Microscopically, during each PWM period, there is a negative battery current, which is caused by the current fluctuations in the d-axis caused by PI regulation. Macroscopically, the battery current is positive, indicating discharge. When the vehicle is stopped, the battery current is close to zero. When the temperature-locking strategy is in effect, a large magnitude of AC can be immediately generated on the battery DC link. Its peak-to-peak values can reach up to 200 A. More importantly, this AC can be superimposed on the normal operating current without affecting the speed tracking of the motor. As can be seen in Figure 19c, the battery voltage is always maintained between 225 and 378 V. Even in the 50th~70th s, the battery voltage does not exceed the upper and lower limits when the battery not only needs to power the motor but also to heat itself. This is due to the fact that, under the effect of the voltage-limiting control strategy, b_n has been called back to 0 many times so that the voltage falls back to the safe range in time.

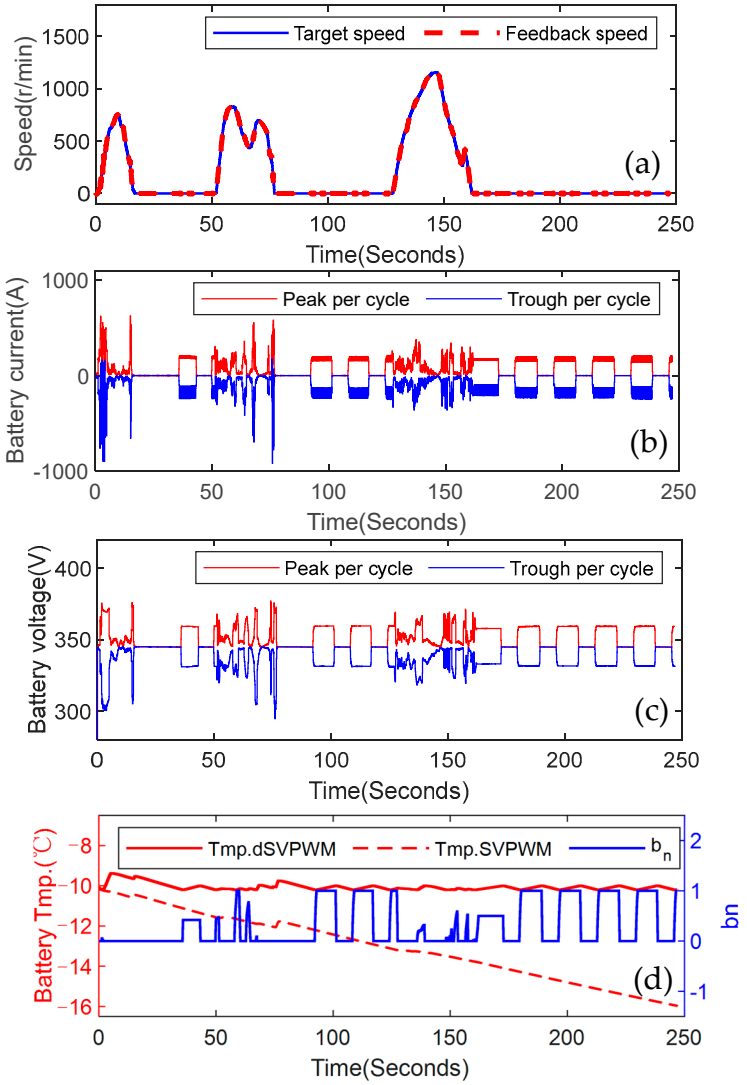

Figure 19. Simulation results using a fragment of the CLTC condition: (**a**) motor speed, (**b**) battery current, (**c**) battery voltage, (**d**) battery temperature and b_n.

As shown in Figure 19d, the third and fourth pulses of b_n between 50 and 70 s are caused by voltage exceeding the upper limit. This implies that the temperature-locking with voltage-limiting strategy is effective in real driving conditions. The average battery temperature plotted in Figure 19d rises significantly after the start of the first driving—stopping cycle, where the heating intensity is zero. When the vehicle stopped for the first time, battery temperature dropped to −10.2 °C around the 35th s, triggering the temperature

locking strategy, and the b_n rose to 0.4. Then, when the temperature reached −9.8 °C, the b_n dropped back to 0. In addition, it is noteworthy that in the third driving–stopping cycle, although the vehicle was driving, it was not possible to maintain its battery temperature due to the small current, so the temperature locking strategy was repeatedly activated, locking the battery temperature above −10 °C at all times. Throughout the extended standstill phase, the temperature-locking strategy is repeatedly activated, resulting in the battery temperature fluctuating between ±0.2 °C. This maintains the vehicle's readiness for immediate startup. In short, the temperature-locking strategy successfully locked the lowest battery temperature at around −10 °C. In contrast, the temperature of the no-lock strategy, as shown by the red dotted line in Figure 19d, generally decreased from −10 °C to −16 °C, which was obviously unable to maintain the normal operation of the battery in an extremely cold environment.

4.2.7. Calculation and Discussion of Energy Balance and Battery Heating Efficiency

According to the aforementioned analysis, the proposed dSVPWM algorithm does not change the magnitude and direction of the FOC vector at the micro level, and the maximum modulation is consistent with the SVPWM algorithm. At the same time, the proposed method does not alter the structure of the motor's stator and rotor. Therefore, the proposed control strategy does not reduce the efficiency of motor control. Fundamentally, the efficiency of transmuting electrical energy stored in the battery into mechanical energy persists unaltered. Upon examining the aspect of battery heating, the primary concern evolves to the effectiveness of converting electrical energy into the internal energy encapsulated within the battery.

According to the law of energy conservation, the electrical energy stored in the battery gradually decreases throughout the self-heating process. This electrical energy can be divided into two parts: one part is converted into electromagnetic energy, which is used to drive the motor, and the other part is used for heating the battery. The emphasis of this study is on the electrical energy allocated for heating the battery. This segment of electrical energy is partly transformed into the battery's internal energy, which serves to elevate the battery's temperature, whereas some of this internal energy is dissipated into the surrounding environment via heat exchange at the battery's surface. The remaining electrical energy is converted into heat energy via the equivalent resistance of the external circuitry.

Based on this, the article defines the heating efficiency as follows:

$$\eta_{heat} = \frac{Q_{ine}}{E_{ele}} = \frac{Q_{ine}}{Q_{ine} + Q_{dis} + Q_{cct}} \tag{16}$$

where in Q_{ine} represents the increment of internal energy of the battery, E_{ele} represents the diminishment of the battery's electrical energy attributable to the heating process, Q_{dis} represents the heat dissipation of the battery, and Q_{cct} represents the heat production from the external circuit.

E_{ele} can be calculated according to the battery open-circuit voltage-capacity curve, as shown in the following equation:

$$E_{ele} = \int_{Q_0}^{Q_{eoh}} u_{ocv} dQ \tag{17}$$

Among them, Q_0 represents the battery capacity at the start of heating, Q_{eoh} represents the battery capacity at the end of heating, and u_{OCV} represents the battery open-circuit voltage corresponding to different capacities. Therefore, as long as the SOC of the battery before and after heating is known, the battery's energy consumption can be obtained.

Q_{ine} can be calculated according to the following equation:

$$Q_{ine} = c_b m_b (T_{eoh} - T_0) \tag{18}$$

wherein c_b represents the total specific heat capacity of the battery, m_b represents the mass of the battery, T_0 represents the initial temperature of the battery, and T_{eoh} represents the temperature at the end of battery heating.

Q_{dis} can be calculated according to the following equation:

$$Q_{dis} = \int_0^{t_{eoh}} hA(T_b - T_{amb})dt \tag{19}$$

Here, h represents the surface heat transfer coefficient, *A* represents the surface area of the battery, T_b represents the average temperature of the battery surface at time t, T_{amb} represents the ambient temperature, and t_{eoh} represents the time used for heating.

Assuming in a PWM cycle, a non-zero vector acts for t_{act} seconds, followed by the insertion of a dead-zone vector for t_{dead} seconds. The calculation equation for Q_{cct} is as follows:

$$Q_{cct} = \frac{3}{2}\int_0^{t_{act}} i_{dc}^2(R_{on} + R_s)dt + \frac{3}{2}\int_{t_{act}}^{t_{act}+t_{dead}} i_{dc}^2 R_s dt + 2\int_0^{t_{act}+t_{dead}} i_b^2 R_{pl} dt \tag{20}$$

In this equation, i_{dc} represents the DC-link current, i_b represents the battery current, R_{on} represents the on-resistance of the MOSFET, R_s represents the phase resistance of the motor, and R_{pl} represents the equivalent ohmic resistance of a single DC-link. The calculation of Q_{cct} above does not take into account the parasitic resistance of the DC-link capacitor because its magnitude is small.

Based on the aforementioned equation, it is evident that the heating efficiency is related to the degree of surface insulation of the battery and the real part of the impedance of the external circuit of the battery. Assuming the surface insulation of the battery is good, the real part of the external circuit impedance becomes the key indicator for evaluating the heating efficiency. The ohmic impedance of a single cell between −30 and −10 °C is approximately between 20 and 35 mΩ, which is more than twice its normal temperature impedance. Since the series number of the battery pack is often much greater than the parallel number, the total impedance of the battery pack increases by an order of magnitude on the basis of the cell impedance. For example, a 380 V battery pack requires 102 series of NCM cells. Assuming the parallel number is 3, its total ohmic internal resistance would be between 680 and 1190 mΩ. In comparison, the equivalent resistance of the external circuit is limited in both value and quantity and is not highly sensitive to temperature. For example, the on-state resistance of an efficient MOSFET is about 3 mΩ, the phase resistance of the motor is about 15 mΩ, and the equivalent resistance of the DC-link is also around 10 mΩ. Therefore, the reduction of electrical energy in the battery during heating is mostly applied to the battery's ohmic internal resistance to increase the battery's own temperature. Based on the above example data, under the condition of battery insulation, the heating efficiency will reach between 95.8% and 97.6%. The primary determinant of heating efficiency is the degree of insulation condition present on the battery's surface.

From the above analysis, it is clear that the majority of the electrical energy reduction during the battery heating process is used for self-heating. The increase in the battery's internal energy can be calculated using Equation (18), and by combining this with the heating efficiency derived from the analysis, the reduction in the battery's State of Charge (SOC) during the heating process can be estimated. Taking the battery sample studied in Section 2.4 as an example, at environmental temperature and the initial battery temperature of −30 °C, heating up to −10 °C results in an internal energy increase of approximately 0.25 Wh per cell. Assuming a heating efficiency of 96%, the total energy consumption for the heating process is about 0.26 Wh. If the open-circuit voltage during the heating process is assumed to be around the rated value of 3.7 V, the equivalent capacity consumption would be approximately 70.27 mAh, which translates to a SOC decrease of 2.81%. Similarly, if the temperature is increased from −30 °C to 0 °C, the SOC decrease can be calculated to be 4.22%. It is worth noting that the heating efficiency estimated by the above method

does not account for the iron losses in the motor because it is much smaller than the loss of copper.

To conduct a more detailed quantitative analysis of the energy distribution relationship for the proposed method, a code was developed to compute the battery thermal power and motor output power within the vehicle-level simulation model detailed in Section 3.2 while simultaneously tracking the SOC consumption of the battery. Utilizing the same configuration and driving conditions, the proposed battery temperature-locking method was implemented. The computational outcomes indicate that the vehicle's total range, based on speed integration, is 189.6 m. The SOC of the battery diminished by 0.065%, starting from 75%. By integrating the battery's open circuit voltage curve at -10 °C, that equates to an energy loss of 22.9 Wh. Dividing this by the distance traveled yields a power consumption of 120.8 Wh/km. Concurrently, the total thermal energy produced by the battery amounts to 2 Wh, encompassing both the energy utilized for battery heating and the heat dissipated to the surroundings. It is equivalent to an energy consumption of 10.5 Wh/km, constituting 8.7% of the overall energy consumption. The motor's mechanical energy output is 19.5 Wh, dedicated to propelling the vehicle, with its energy consumption at 102.8 Wh/km, representing 85.1% of the total energy consumption. The residual energy consumption is primarily attributed to the parasitic resistance of the inverter, motor coil, and DC-link. It is worth noting that this simulation does not account for the energy consumption of other electrical or mechanical loads on the vehicle and is representative solely of the -40 °C low-temperature environment and low-speed driving conditions within the CLTC cycle.

5. Conclusions

This paper focuses on the problem that the battery temperature cannot be maintained when the electric vehicle is running in extremely cold environments and low-speed conditions. The dead zone is introduced into the SVPWM algorithm for driving PMSM to form the newly proposed dSVPWM algorithm, which is used to reconstruct the dual-PI control model with an FOC control strategy and theoretically opens up a new technical path to realize the battery AC self-heating while driving based on the topology of the existing electric drive system. With the help of voltage vector synthesis, it is proved that the replacement of part of the zero vector in the original SVPWM algorithm with the dead-zone vector and the compensation vector in the dSVPWM algorithm does not change the original output voltage vector, and the amplitude of the battery AC can be changed by adjusting the heating intensity defined by the ratio of the dead zone and the compensation vector to the original zero vector. With the help of the Simulink model and the small-scale motor driving system test bench, the simulation and experimental comparison of the motor control algorithm based on dSVPWM was carried out. Firstly, it is found that the battery current amplitude calculated by the model was consistent with the experimental value under three target speeds using the original SVPWM algorithm, which verifies the precision of the numerical model and PI parameters. Secondly, the heating intensity was changed from 0 to 0.5 in the constant speed test. The comparison between the two figures indicated that an obvious AC battery current was formed, with its amplitude increasing from 1.8 A to 4.4 A, and the motor speed could be kept stable, which verified the controllability of the dSVPWM algorithm on the battery AC. Then, the dSVPWM and SVPWM algorithms were compared and studied in the numerical model, and it is concluded that the dSVPWM algorithm can obtain up to double the peak-to-peak alternating battery current at medium and high speeds, and although the dSVPWM algorithm produces additional motor phase current and torque ripple positively correlated with heating intensity under the same working conditions, it retains excellent resistance to load torque disturbances across a range of target speeds and varying levels of heating intensity, which proves that the proposed algorithm possesses adequate stability. Finally, a structure and workflow for the temperature-locking strategy are given, and the goal is to lock the battery temperature within the set thresholds and avoid the battery voltage overrun. Combined with the parameters of a passenger car provided by

the vehicle manufacturer, the proposed temperature locking strategy was deployed into the numerical model of the motor driving system. The study investigated the control effect of the temperature locking strategy on the voltage, current, and temperature of the vehicle power battery under CLTC urban conditions, comparing the battery temperature with that observed under a strategy without temperature locking. It is concluded that (1) the temperature-locking strategy effectively prevents the average battery temperature from declining during urban low-speed driving conditions. Without this strategy, the average battery temperature decreases by 1.44 °C per minute. (2) the strategy ensures precise speed tracking in urban low-speed driving conditions while maintaining the battery temperature within specified upper and lower thresholds. The average temperature fluctuation remains within 1 °C. (3) with the heating function activated, the strategy effectively prevents battery voltage from exceeding safe limits, ensuring the battery's safe operation. In conclusion, the above theories and methods proposed in this paper open up a new feasible technical route for the battery AC self-heating during vehicle driving, and based on this, how to realize the battery AC self-heating coupling with other senior motor control strategies can be further studied.

This paper merely expounds on the fundamental principles of the proposed methodology, accompanied by an initial validation of its feasibility through preliminary examination. Future research endeavors can be pursued in the following aspects: Firstly, incorporate temperature-sensitive parameters of the motor and controller into the simulation model, thereby constructing a heightened comprehensive temperature-adaptive simulation and calculation platform. This platform will facilitate an in-depth examination of the performance characteristics and temperature variations exhibited by the motor and inverter within extremely cold environments. Secondly, embark on a spectral analysis of current and torque data, aiming to meticulously analyze the impact of this methodology on motor torque fluctuations and NVH phenomena, adopting a frequency domain approach for a more profound understanding. Furthermore, from a rigorous energy balance perspective, a quantitative analysis will be conducted to elucidate the relationship between motor drive efficiency and heating efficiency, along with a thorough examination of other intricately related issues.

Author Contributions: Conceptualization, W.L.; methodology, W.L.; validation, W.L. and W.S.; investigation, W.L.; data curation, W.L.; writing—original draft preparation, W.L.; writing—review and editing, W.L.; visualization, W.L.; software, W.L. and W.S.; formal analysis, W.S.; resources, S.X.; supervision, S.X.; administration, S.X.; funding acquisition S.X.; project, S.X. All authors have read and agreed to the published version of the manuscript.

Funding: This research was funded by the Open Foundation for Key Laboratory of Clean Energy and Carbon Neutrality of Zhejiang Province grant number [204022023005A] and Zhejiang Province Spearhead and Leading Goose Research and Development Key Program grant number [2023C01239].

Data Availability Statement: The original contributions presented in the study are included in the article, further inquiries can be directed to the corresponding author.

Conflicts of Interest: The authors declare no conflict of interest.

References

1. Lee, D.Y.; Cho, C.W.; Won, J.P.; Park, Y.C.; Lee, M.Y. Performance characteristics of mobile heat pump for a large passenger electric vehicle. *Appl. Therm. Eng.* **2013**, *50*, 660–669. [CrossRef]
2. Qin, F.; Xue, Q.; Albarracin Velez, G.M.; Zhang, G.; Zou, H.; Tian, C. Experimental investigation on the heating performance of heat pump for electric vehicles at −20 °C ambient temperature. *Energy Convers. Manag.* **2015**, *102*, 39–49. [CrossRef]
3. Zhu, J.; Sun, Z.; Wei, X.; Dai, H.; Gu, W. Experimental investigations of an AC pulse heating method for vehicular high power lithium-ion batteries at subzero temperatures. *J. Power Sources* **2017**, *367*, 145–157. [CrossRef]
4. Jaguemont, J.; Boulon, L.; Dubé, Y. A comprehensive review of lithium-ion batteries used in hybrid and electric vehicles at cold temperatures. *Appl. Energy* **2016**, *164*, 99–114. [CrossRef]
5. Zhang, J.; Ge, H.; Li, Z.; Ding, Z. Internal heaating of lithium-ion batteries using alternating current based on the heat generation model in frequency domain. *J. Power Sources* **2015**, *273*, 1030–1037. [CrossRef]

6. Zhu, J.; Sun, Z.; Wei, X.; Dai, H. An alternating current heating method for lithium-ion batteries from subzero temperatures. *Int. J. Energy Res.* **2016**, *40*, 1869–1883. [CrossRef]
7. Ruan, H.; Jiang, J.; Sun, B.; Zhang, W.; Gao, W.; Wang, L.Y.; Ma, Z. A rapid low temperature internal heating strategy with optimal frequency based on constant polarization voltage for lithium-ion batteries. *Appl. Energy* **2016**, *177*, 771–782. [CrossRef]
8. Li, J.; Sun, D. Lithium-ion Batteries Modeling and Optimization Strategies for Sinusoidal Alternating Current Heating at Low Temperature. *Energy Procedia* **2018**, *152*, 562–567. [CrossRef]
9. Li, J.-Q.; Fang, L.; Shi, W.; Jin, X. Layered thermal model with sinusoidal alternate current for cylindrical lithium-ion battery at low temperature. *Energy* **2018**, *148*, 247–257. [CrossRef]
10. Jiang, J.; Ruan, H.; Sun, B.; Wang, L.; Gao, W.; Zhang, W. A low-temperature internal heating strategy without lifetime reduction for large-size automotive lithium-ion battery pack. *Appl. Energy* **2018**, *230*, 257–266. [CrossRef]
11. Guo, S.; Xiong, R.; Wang, K.; Sun, F. A novel echelon internal heating strategy of cold batteries for all-climate electric vehicles application. *Appl. Energy* **2018**, *219*, 256–263. [CrossRef]
12. Guo, S.; Xiong, R.; Sun, F.; Cao, J.; Wang, K. An echelon internal heating strategy for lithium-ion battery. *Energy Procedia* **2017**, *142*, 3135–3140. [CrossRef]
13. Ruan, H.; Jiang, J.; Sun, B.; Wu, N.; Shi, W.; Zhang, Y. Stepwise segmented charging technique for lithium-ion battery to induce thermal management by low-temperature internal heating. In Proceedings of the 2014 IEEE Conference and Expo Transportation Electrification Asia-Pacific (ITEC Asia-Pacific), Beijing, China, 31 August–3 September 2014; IEEE: New York, NY, USA, 2014.
14. Guo, S.; Xiong, R.; Shen, W.; Sun, F. Aging investigation of an echelon internal heating method on a three-electrode lithium-ion cell at low temperatures. *J. Energy Storage* **2019**, *25*, 100878. [CrossRef]
15. Shang, Y.; Xia, B.; Cui, N.; Zhang, C.; Mi, C.C. An Automotive Onboard AC Heater Without External Power Supplies for Lithium-Ion Batteries at Low Temperatures. *IEEE Trans. Power Electron.* **2018**, *33*, 7759–7769. [CrossRef]
16. Shang, Y.; Zhu, C.; Fu, Y.; Mi, C.C. An Integrated Heater Equalizer for Lithium-Ion Batteries of Electric Vehicles. *IEEE Trans. Ind. Electron.* **2019**, *66*, 4398–4405. [CrossRef]
17. Shang, Y.; Liu, K.; Cui, N.; Zhang, Q.; Zhang, C. A Sine-Wave Heating Circuit for Automotive Battery Self-Heating at Subzero Temperatures. *IEEE Trans. Ind. Inform.* **2020**, *16*, 3355–3365. [CrossRef]
18. Shang, Y.; Liu, K.; Cui, N.; Wang, N.; Li, K.; Zhang, C. A Compact Resonant Switched-Capacitor Heater for Lithium-Ion Battery Self-Heating at Low Temperatures. *IEEE Trans. Power Electron.* **2020**, *35*, 7134–7144. [CrossRef]
19. Zhang, Y.; Yang, Y.; Shang, Y.; Cui, N. A high frequency AC heater based on switched capacitors for lithium-ion batteries at low temperature. *J. Energy Storage* **2021**, *42*, 102977. [CrossRef]
20. Zhu, C.; Zhang, H.; Lu, F. A Compact Onboard Battery Self-Heater for All-Electric Aircraft Applications at Cold Climates. In Proceedings of the 2019 IEEE National Aerospace and Electronics Conference (NAECON), Dayton, OH, USA, 15–19 July 2019; IEEE: New York, NY, USA, 2019.
21. Zhu, C.; Shang, Y.; Lu, F.; Zhang, H. Optimized Design of an Onboard Resonant Self-Heater for Automotive Lithium-Ion Batteries at Cold Climates. In Proceedings of the 2019 IEEE Energy Conversion Congress and Exposition (ECCE), Baltimore, MD, USA, 29 September–3 October 2019; IEEE: New York, NY, USA, 2019.
22. Zhu, C.; Cao, Y.; Zhang, H.; Lu, F.; Zhang, X. Comprehensive Design and Optimization of an Onboard Resonant Self-Heater for EV Battery. *IEEE Trans. Transp. Electrif.* **2021**, *7*, 452–463. [CrossRef]
23. Baba, H.; Kawasaki, K.; Kawachi, H. *Battery Heating System for Electric Vehicles*; SAE Technical Paper Series; SAE: Warrendale, PA, USA, 2015.
24. Li, Y.; Gao, X.; Qin, Y.; Du, J.; Guo, D.; Feng, X.; Lu, L.; Han, X.; Ouyang, M. Drive circuitry of an electric vehicle enabling rapid heating of the battery pack at low temperatures. *iScience* **2021**, *24*, 101921. [CrossRef]
25. Li, Y.; Du, J.; Zhou, G.; Ouyang, M.; Fan, Y. A rapid self-heating battery pack achieved by novel driving circuits of electric vehicle. *Energy Rep.* **2020**, *6*, 1016–1023. [CrossRef]
26. Zhu, C.; Han, J.; Guo, B.; Fan, G.; Zhang, X. A Split-Source Self-Heater for Automotive Batteries Based on Traction Drive Reconfiguration. *IEEE J. Emerg. Sel. Top. Ind. Electron.* **2023**, *4*, 188–197. [CrossRef]
27. Du, C.; Peng, Q.; Chen, F.; Deng, K.; Chen, J.; Deng, C.; Hu, M. Investigation on the method of battery self-heating using motor pulse current. *Proc. Inst. Mech. Eng. Part D J. Automob. Eng.* **2022**, *236*, 2399–2409. [CrossRef]
28. Li, W.; Shi, W.; Xiong, S.; Huang, H. Voltage-feedback Internal Heating Strategy of Lithium-Ion Battery in an Extremely Cold Environment Implemented with Drive System of Electric Vehicle. *IEEE Trans. Transp. Electrif.* **2023**. [CrossRef]
29. Yuan, L.; Hu, B.; Wei, K.; Chen, Z. *Modern Permanent Magnet Synchronous Motor Control Principle and MATLAB Simulation*; Beihang University Press: Beijing, China, 2016.
30. Harnefors, L.; Pietilainen, K.; Gertmar, L. Torque-maximizing field-weakening control, design, analysis, and parameter selection. *IEEE Trans. Ind. Electron.* **2001**, *48*, 161–168. [CrossRef]